world

MDPI

Article

Spatiotemporal Modeling and Prediction of Urban Thermal Field Variation and Land Use Dynamics in Riyadh Using Machine Learning and Remote Sensing

Md Tanvir Miah [1], Raiyan Raiyan [1], Ayad Khalid Almaimani [2] and Khan Rubayet Rahaman [3,*]

[1] Urban and Rural Planning Discipline, Khulna University, Khulna 9208, Bangladesh; tanvir180417@gmail.com (M.T.M.); raiyanrockers@gmail.com (R.R.)
[2] Architecture Department, Faculty of Architecture and Planning, King Abdulaziz University, Jeddah 21589, Saudi Arabia; ealmaimani@kau.edu.sa
[3] Department of Geography and Environmental Studies, St. Mary's University, Halifax, NS B3H 3C3, Canada
* Correspondence: khan.rahaman@smu.ca

Abstract

Urban areas in arid environments are increasingly affected by the urban heat island (UHI) effect, which intensifies thermal stress, disrupts ecological balance, and poses challenges for sustainable urban development. Understanding and predicting spatiotemporal variations in land surface temperature (LST) and land use dynamics is therefore critical for effective urban planning. This study develops a predictive framework for Riyadh, Saudi Arabia, using long-term Landsat time series data (1993–2023) and deep learning models to evaluate urban thermal patterns via the Urban Thermal Field Variation Index (UTFVI). Artificial Neural Networks (ANNs) with six hidden layers for LST and seven for UTFVI forecast future trends up to 2043. The results indicate that urban areas expanded by 521.62 km^2, increasing from 8.73% to 19.56% between 1993 and 2023, and are projected to reach 1509.40 km^2 (25.28%) by 2043, while vegetation coverage declined from 0.771% to 0.674%. The highest average summer LST increased from 56.73 °C in 1993 to 59.89 °C in 2023 and is predicted to rise to 60.79 °C by 2033 and 61.52 °C by 2043. Winter temperatures exhibited a comparable upward trend, rising from 30.75 °C to 32.33 °C in 2023 and projected to reach 34.48 °C by 2043. UTFVI analysis revealed a substantial expansion of weak thermal field zones, which covered 2778 km^2 in 2023 and are expected to reach 3018.44 km^2 (57%) by winter 2043, accompanied by a marked contraction of strong thermal field areas. The ANN models achieved a high predictive performance, with RMSE values of 0.759 (summer) and 0.789 (winter) for UTFVI and correlation coefficients of 0.91 and 0.89, respectively. Projections further indicate that, by 2043, approximately 39.31% of the study area will experience summer temperatures between 48 °C and 53 °C, compared to 5.59% in 2023. These findings highlight the accelerating interaction between urban growth and thermal intensification in arid cities. The proposed modeling framework provides a robust decision-support tool for urban planners and policymakers to mitigate UHI impacts and promote climate-resilient and sustainable urban development.

Keywords: urban thermal dynamics; deep learning prediction; land use change; sustainable urban development; remote sensing; UHI mitigation

Check for updates

Academic Editor: Matthaios Santamouris

Received: 30 January 2026
Revised: 9 March 2026
Accepted: 12 March 2026
Published: 18 March 2026

Copyright: © 2026 by the authors. Licensee MDPI, Basel, Switzerland. This article is an open access article distributed under the terms and conditions of the Creative Commons Attribution (CC BY) license.

1. Introduction

Urban environments worldwide are facing critical challenges stemming from climate variability, with significant impacts on thermal ecology and overall quality of life. The

complex interplay between urban development and climate change has emerged as an important area of research, particularly in rapidly growing cities in arid regions. As urban planners, healthcare professionals, and energy conservationists grapple with these challenges, the need for precise predictions of thermal field fluctuations has grown increasingly pressing [1]. The UTFVI serves as a key indicator of heating and thermal stress in cities, closely linked to the dynamic interplay between urbanization and climate change. Riyadh, the capital city of Saudi Arabia, presents a compelling case study for investigating these urban thermal dynamics. The city's fast urbanization, distinctive meteorological conditions, and considerable socioeconomic growth cultivate a complex environment where the relationships between UTFVI, LULC (Land Use and Land Cover), and LST are particularly pronounced [2–4]. Riyadh's evolution offers valuable insights into the challenges faced by growing urban centers in arid climates worldwide.

LULCC plays a significant role in intensifying global warming and contributing to the formation of UHIs. These changes disrupt ecological balance and directly affect LST, which in turn influences the UTFVI. In Riyadh, rapid urbanization and industrial expansion have converted over 35–40% of natural vegetation to built-up areas between 1990 and 2020 [5,6]. These transitions have led to an average LST increase of 4–6 °C in urbanized zones compared to surrounding rural areas, demonstrating a pronounced UHI effect [7]. Studies also indicate that urban areas contribute nearly 70% of local heat anomalies during summer months, highlighting the impact of LULCC and seasonal fluctuations on the thermal landscape. The impermeable urban surface not only raises LST but also diminishes ecological resilience, creating a feedback loop that exacerbates environmental degradation and presents major challenges for urban planning and sustainable development.

UTFVI, which links land use and surface temperature, is an important tool in studying city climates. It helps measure heat stress and comfort in urban areas and shows how cities affect the environment. A high UTFVI is associated with more emissions, fewer natural resources, lower biodiversity, and stronger urban heat effects. Because of this, UTFVI is increasingly used to assess urban well-being and sustainable growth. Saudi Arabia is seeing new planned cities alongside traditional ones. If land use is not managed well, these developments can cause problems. While they boost the economy, they also change land cover, surface temperature, and thermal patterns, affecting the city's UTFVI. Studies in Riyadh show that unplanned growth without more green spaces or water can steadily raise temperatures, making some areas hard to live in. These findings underscore the crucial importance of focusing on LULC, LST, and their impacts on UTFVI to mitigate urban heat and prevent the formation of UHIs [8,9].

In addition, the geothermal variation in urban areas, as measured by UTFVI, is a critical metric for assessing the detrimental impacts of the urban warming effect [10]. The higher levels of geothermal variation in towns and cities, caused by urbanization and reflected in UTFVI values, result in warmer weather compared to nearby rural areas [11]. This phenomenon has wide-ranging effects on local atmospheric conditions, reduced air quality, substantial economic losses, decreased comfort, and elevated mortality rates [12]. Furthermore, the UHI effect, closely related to UTFVI, contributes to more frequent precipitation and rainstorms, as the intense heat generates powerful ascending air masses [13]. These interconnected environmental challenges highlight the need for the accurate predictions of UTFVI changes to identify potential extreme heat hotspots and develop effective methods to minimize the UHI effect [14].

These studies show important links between land use changes, surface temperature, and UTFVI, helping cities plan eco-friendly systems. The integration of advanced technologies and methodologies, such as Geographic Information Systems (GISs) and remote sensing (RS) techniques, has enabled the development of highly accurate spatially explicit

models. These include Cellular Automata (CA) [15,16] and Artificial Neural Networks (ANNs) [17], which have proven effective in estimating future urban conditions and their impacts on UTFVI. The importance of these forecasting models in predicting UTFVI changes cannot be overstated. Without them, urban planners and policymakers risk making decisions without crucial information, potentially exacerbating UHI effects and thermal flux diversity. The consequences of failing to incorporate these forecasting strategies into city development methods could be severe, leading to disastrous ecological damage, humanitarian difficulties, and lasting harm to urban ecology [18]. These prediction models play a crucial role in preventing negative outcomes that might result from uncontrolled urbanization and environmental deterioration [19].

In light of these challenges and the critical need for effective urban thermal management strategies, this study aims to develop a robust machine learning framework to accurately forecast seasonal variations in UTFVI for Riyadh. The primary objectives of this research are:

(a) To develop and implement advanced machine learning algorithms for predicting UTFVI changes in Riyadh, incorporating LULC and LST data.
(b) To analyze the complex relationships between LULCC, LST variations, and UTFVI patterns in the context of Riyadh's rapid urban growth.
(c) To quantify the impact of urban expansion and land use changes on UTFVI and thermal stress levels in Riyadh.
(d) To provide actionable insights and recommendations for sustainable urban planning and climate adaptation strategies based on UTFVI predictions and their relationship to LULC and LST.

The uniqueness of this study lies in its comprehensive approach to integrating UTFVI, LULC, and LST analyses using advanced machine learning techniques. By focusing on the interrelationships between these factors in the context of a rapidly growing desert city, this research fills a critical gap in our understanding of urban thermal dynamics in arid regions. The significance of this research extends beyond academic circles. It has the potential to provide actionable insights for urban planners, climate safety professionals, and policymakers. By offering practical recommendations based on the relationship between UTFVI, LULC, and LST, this study aims to enhance thermal comfort and overall quality of life in Riyadh. Moreover, the methodologies and findings of this research have broader applicability to other rapidly urbanizing cities facing similar thermal challenges, particularly in arid regions. As cities worldwide grapple with the impacts of climate change and rapid urbanization, the lessons learned from Riyadh's experience can contribute significantly to the global discourse on sustainable urban development and climate resilience. By providing a comprehensive understanding of how UTFVI changes in response to LULC and LST variations, this study will equip decision-makers with the tools and knowledge necessary to create more sustainable, livable urban environments in the face of ongoing climate challenges.

2. Materials and Methods

2.1. Study Area

The city of Riyadh, which serves as the state capital of Saudi Arabia, is situated in an important location in the middle of the kingdom of Saudi Arabia, at nearly 24.7136° N latitude and 46.6753° E longitude [20]. Riyadh has a vast area of around 5969 km^2 and is distinguished by its varied terrain, which includes valleys, steep escarpments, sandy desert plains, and flat desert plains. The region of Riyadh is a substantial urban hub that has a substantial amount of influence over the areas that are located in close proximity due to its exceptional geographical location on a hilltop in the middle of the kingdom [21].

In accordance with the [22] climatic classification, Riyadh is characterized by a hot, dry climate, which is specifically designated as "BWH". Hot temperatures in the summer, which often go beyond 45 °C, and pleasant to cold winters, with temperatures ranging from 8 °C to 20 °C, are the defining characteristics of this climate. The city gets a little amount of precipitation on a yearly basis, which is often less than 100 mm. This precipitation usually occurs in short, scattered showers throughout the shifting season of summer and fall. A considerable contribution to the UHI impact is made by dry climates and high heat waves, which in turn exacerbate the heat stress that the people who live in the city are experiencing [23].

As shown in Figure 1, Riyadh, the political and economic capital of Saudi Arabia, is a major regional center with diverse sectors including government services, finance, trade, and manufacturing, contributing to the GDP under Vision 2030 for economic diversification [24]. Rapid urbanization and infrastructure investments reinforce its role as an economic hub. Geologically, it lies on the Najd Plateau, underlain by sedimentary rocks such as limestone, shale, and marl from the Paleozoic–Cenozoic eras [25].

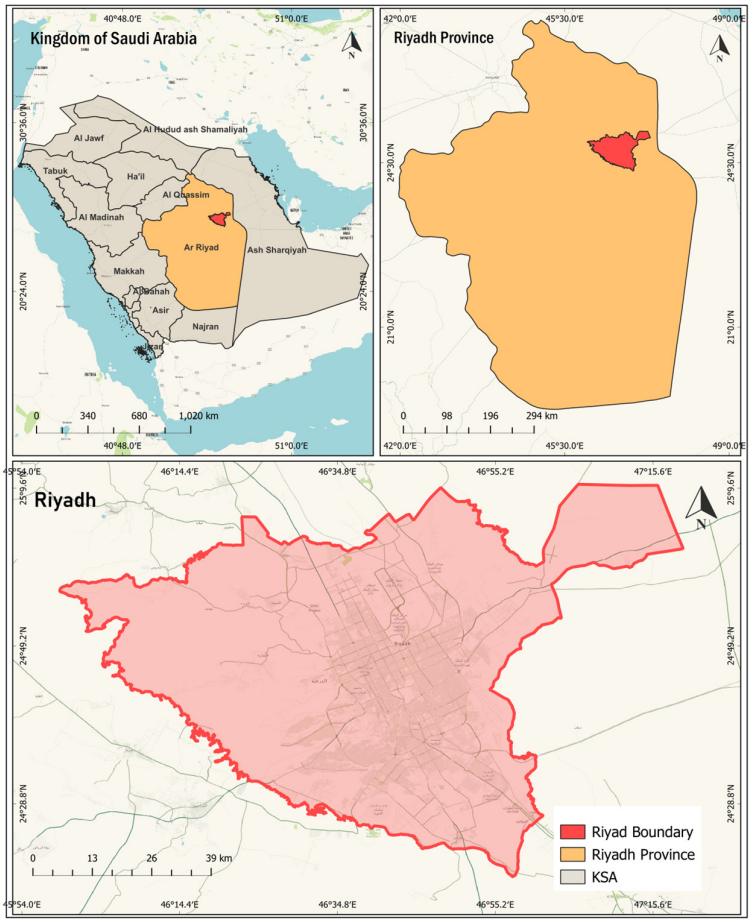


Figure 1. Study area map.

The urban area of Riyadh has been gradually expanding due to seasonal expansion and large immigration, making it one of the cities in Saudi Arabia and the Middle East that is seeing the most rapid expansion. A diversified citizenry that is looking for work and business possibilities is drawn to the city since it is a significant economic and organizational hub. According to the most current projections, Riyadh has a population that is more than seven million, making it the most populous town in the kingdom for demographics [26]. Large-scale urban development, which is defined by the expansion of residential, commercial, and industrial sectors, is occurring concurrently with the fast

increase in the population. Due to the alteration of Riyadh's geography brought about by urbanization, the effect of UHI has become more pronounced [27]. This phenomenon occurs when urban regions suffer greater temperatures than their rural surroundings. As a result of the expanding heat island phenomenon and the dry climate of the city, there is a potential threat to public health, energy consumption, and general desirability. The city of Riyadh is an interesting case study for analyzing urban thermal dynamics in dry environments due to its distinctive geographical, climatic, and urbanization features.

2.2. Methods

USGS has triple multi-spectral Landsat 5 TM and Landsat 8 OLI satellite images from 1993 to 2023 for examining LULC and LST changes' effects on UTFVI in the research area. However, various methodological errors exist. Despite using winter and summer images to reduce temporal variations, this strategy fails to account for intra-seasonal variability. The idea that one month's data may reflect seasonal fluctuations is erroneous. Also, "almost nonexistent" cloud cover is an imprecise and unproven assertion; hence, the requirement that it be less than 10% is imprecise and insufficient. Assumptions that geo-correction or image-by-image manipulation is unnecessary because Landsat images are naturally devoid of radiometric and geometrical error ignore prospective issues with data quality that can develop in satellite imagery, like atmospheric disturbances or malfunctioning sensors. In addition, according to [28], resizing all Landsat infrared bands to 30 m causes temporal inconsistencies and reprocessing artifacts, which might impact data integrity. Table 1 summarizes the USGS online database, which this technique relies on. This fact alone eliminates the need for a comprehensive validation procedure, which is necessary to guarantee that the data utilized in this research are accurate and reliable.

Table 1. Details of the datasets used in this study.

Duration	Dataset	Bands	Detector	Geospatial Resolution
1993	Phase 2 Landsat 5 data, Acquisition 2 Tier 1	1 to 7	Landsat 5 TM	30
2003	Phase 2 Landsat 5 data, Acquisition 2 Tier 1	1 to 7	Landsat 5 TM	30
2013 2023	Phase 2 Landsat 8 data, Acquisition 2 Tier 1	2 to 7	Landsat 8 OLI	30

2.3. Data Collection and Processing

As per the study conducted by [29], we utilized satellite images obtained from the US Geological Survey (USGS) through the Earth Explorer platform. However, Table 1 presents the imagery captured by Landsat 4/5 TM data in 1993 and by Landsat-8 OLI data in 2003, 2013, and 2023. These four years were selected to represent three decades of urban and environmental change based on the availability of high-quality, cloud-free imagery at roughly 10-year intervals, allowing for a consistent temporal analysis of long-term trends. The selection also ensured that images were comparable in terms of sensor characteristics and spatial resolution, minimizing potential biases in the interpretation of land cover and thermal patterns.

The data's accuracy was ensured through a series of image preprocessing steps, including adjustments for geometric, atmospheric, and radiometric factors. Terrain, solar angle, atmospheric effects, and geographic positioning were considered during the spectrum calibration phase to enhance data reliability. Layer alignment and image clipping were applied to match the study area boundaries. Additionally, a digital elevation model (DEM)

from the USGS was integrated into ArcGIS Pro 3.4 for the precise mapping and analysis of landscape features, further improving the understanding of geographical dynamics in the study area [30,31].

2.3.1. Classification of LULC Images

Using machine envision detection, which has been shown to be reliable and easy to use, the inquiry spanned from 1993 to 2023. Regarding the selection of only four years to represent a 30-year period, we would like to clarify that these years (1993, 2003, 2013, and 2023) were carefully chosen based on the availability of cloud-free Landsat imagery with consistent quality, which is essential for accurate LST and land use/land cover analysis. Additionally, these years are evenly spaced at approximately 10-year intervals, allowing for a representative assessment of long-term spatiotemporal trends in urbanization and thermal dynamics. Images require being accurately classified and organized into the right categories in order to train classifiers, as pointed out by [32].

Separating the wavelength patterns of different LULC classes using bounding circles was the first step in preparing the supervised machine learning algorithm that would later be used for each class's training set. Using the Random Forest (RF) algorithm in GEE, a supervised image classification was performed. Over 500 points per land class were collected on average, with 70% allocated for model training and 30% for validation. The input features included the Landsat spectral bands (Blue, Green, Red, Near-Infrared, SWIR1, and SWIR2), which provide sufficient spectral information for distinguishing major land use types. The land use categories that were intended to be classified were roadways, pavements, construction sites, and industrial zones, all examples of built-up regions that commonly employ inert gravel. Vegetation is characterized by a variety of plant life, including palm trees, Apple of Sodom, lush vegetation, canopy thorn, and pencil cactus. Unoccupied regions, rocks, and barren landscapes are all part of bare land. According to Table 2, ArcGIS Pro 3.4 was used to perform the LULC categorization. Points for each land cover class were carefully and randomly selected to enhance the validation process. The correctness and reliability of the classification were checked by cross-referencing these sites with Google Earth images. In order to ensure that the final results could be relied on, this thorough multi-step validation process was necessary. Despite the methodical approach, there are still important factors to consider: The reliability and accuracy of the images used to train the classifier are crucial to its success. The accuracy of the classifier can be severely compromised by differences in picture resolution, gaps in time, or contradictory data sources. Drawbacks of the algorithm: The heterogeneity within each portion of land class may not be completely captured when training sets are prepared using bounding circles. Classification accuracy may be improved with the use of more sophisticated segmentation methods. Throughout the time period covered by the study, which begins in 1993 and ends in 2023, there have been substantial shifts in the portion of land cover.

Table 2. Details of LULCC.

LULC Type	Details
Built-Up	On roadways pavement, building sites, and around industries, inert gravel is often paved over.
Vegetation	Palm trees, Apple of Sodom, verdant landscapes, and scattered areas that comprise botanical variety; umbrella thorn; pencil cactus.
Bare Land	Rocks, deserted terrain, and uninhabited areas.

2.3.2. Accuracy Assessment

Accurate evaluation is necessary for systems that use images. The first investigations often involved comparing ground-truth data or specific locations on classified maps [33]. GEE has confirmed those maps for the years 1993, 2003, 2013, and 2023. Equations (1)–(3) were referenced from [34,35]. We utilized the following formulas to evaluate the accuracy: (1 to 3). The research examines the geographic accuracy of Riyadh municipality regions over a span of 30 years, from 1993 to 2023. The study utilizes recall, accuracy, and the F1-score in conjunction with UA and PA [36,37]. ROC curves are complex yet crucial [38]. Equations (1) and (2) demonstrate the TPR and FPR at different categorization levels with precision. The rates in this graph are connected through specificity along with sensitivity.

$$\mathrm{TPR} = \frac{\text{True Positive}}{\text{True Positive} + \text{False Negative}} \quad (1)$$

$$\mathrm{FPR} = \frac{\text{False Positive}}{\text{Fasle Positive} + \text{True Negative}} \quad (2)$$

$$\mathrm{AUC} = \int_0^1 \mathrm{TPRd}(\mathrm{FPR}) \quad (3)$$

ROC curve categorization is good for proficiency evaluation. The model prefers top-left curves. Calculating the AUC for varied ROC graphs uses Equation (3) [39]. Categorization and research depth grow with AUCs. ROC curves provide dynamic assessment efficiency in difficult calculations.

2.4. Estimation of Seasonal LST

Landsat Collection 2 Level-2 surface reflectance and surface temperature products from Landsat 5, 7+, and 8 were used to ensure radiometrically and atmospherically corrected data. Cloud and shadow masking were performed using the Quality Assessment (QA) band and the CFMask algorithm. For image selection, scenes were filtered based on consistent seasonal periods such as summer and winter months, see Table 3, to maintain the comparability of thermal conditions across years. Additionally, only images with cloud cover below 10% over the study area were selected to minimize atmospheric interference and data gaps. Landsat imagery was used (Table 3) to calculate quarterly LST for 1993, 2003, 2011, and 2023 after infrared band asymmetrical and imaging assessments. (DN) is the format in which Landsat detectors collect data regarding temperatures. There were three stages for Landsat 5 and a long seven-step procedure for Landsat 8 OLI for transforming these DNs to LST in this research. It is unclear whether the resulting LST data can be reliably compared over several Landsat outreaches due to the methodology used. In addition, the LST estimates may be impacted by more closely related difficulties caused by the extensive procedure, which is possibly vulnerable to error conversion, used for Landsat 8 OLI. The validity and transparency of the LST results obtained from these different procedures need a comprehensive review of the study's methods.

Table 3. Listed below is the list of Landsat TM/ETM þ data that were used in this research.

Year	Acquisition Date		Dataset	Bands	Sensor	Spatial Resolution
	Winter	Summer				
1993	11 December	5 April	Stage 2, Landsat 5	1 to 7	Landsat 5 TM	30
2003	7 December	3 April	2 Stage, Landsat 7	2 to 7	Landsat 7 ETM+	30
2013	13 January	17 May				
2023	21 December	11 April	2 Stage, Landsat 8	2 to 7	Landsat 8 OLI	30

2.4.1. Estimation of LST Using Landsat 5 Images

We used the lowest- and highest-temperature data for the study area that were collected from meteorological stations that were managed by the Saudi Arabia Meteorological Department (SAMD) over the course of many years (1993, 2003, 2013, and 2023) in order to validate the precision of the anticipated LST.

Stage 1. The wavelength intensity (R_{TM6}) was calculated from the Strap 6 DNs utilizing the formulas

$$(R_{TM6}) = \frac{V}{255}(R_{max} - R_{min}) + R_{min} \quad (4)$$

where V indicates the DN of band 6, and,

$$R_{max} = 1.896\left(mW \times cm^{-2} \times sr^{-1}\right),\ R_{min} = 0.1534\left(mW \times cm^{-2} \times sr^{-1}\right)$$

Stage 2. The above RTM6 was transformed into LST in K using Equation (5):

$$T_k = \frac{K_1}{Ln(\frac{K_2}{R_{\frac{TM6}{b}}} + 1)} \quad (5)$$

Here, $K_1 = 607.66\left(mW \times cm^{-2} \times sr^{-1}\right)$and $K_2 = 1260.56K$, and b (spectral range) = 1.239 (μm).

Stage 3. The following equation was used in converting the LST from K to °C (6):

$$T_{0c} = T_k - 273 \quad (6)$$

2.4.2. Estimation of LST Using Landsat 8 Imagery

Stage 1. Firstly, we constructed spectrum reflection (SR) images from the primary Landsat-8 data by following the procedures described in [40–42]. This adjustment made utilization of many bands from the Operating Landscape Imager (OLI) and the thermal infrared sensor (TIRS), namely bands 10 and 11.

$$TB = \left(\frac{R_{max} - R_{min}}{DN_{max}}\right) * Band + L_{min} \quad (7)$$

where L = atmospheric SR (watts/m^2 × srad × μm). Lmax = band's highest SR; Lmin = band's minimal SR; the max and min sensor calibration differences are DNmax and Qcal min.

Stage 2. After identifiers had been altered to SR, statistics from the TIRS bands were transformed from SR to BT using detailed file heat factors. Reflection was converted to BT using Equation (8) [28]:

$$BT = \frac{K_2}{Lni(\frac{K_1}{L_\lambda} + 1)} - 273.15 \quad (8)$$

where BT = Celsius brightness temperature, K_1 = 774.89 $\left(mW \times cm^{-2} \times sr^{-1}\right)$, and K_2 = 1321.08 K for band 10; K_1 = 480.89 $\left(mW \times cm^{-2} \times sr^{-1}\right)$ and K_2 = 1201.14 K for band 11.

Stage 3. NDVI estimation is crucial for Landsat 8 LST estimation [43,44]. So NDVI was calculated using Equation (9).

$$NDVI = \frac{NIR(Band\ 5) - R(Band\ 4)}{NIR(Band\ 5) + R(Band\ 4)} \quad (9)$$

with the range −1 < NDVI < +1.

Stage 4. Equation (10) determined the (PV) from lowest and highest NDVI values [45,46]:

$$P_v = \left(\frac{NDVI - NDVImin}{NDVI_{max} - NDVI_{max}}\right)^2 \quad (10)$$

Stage 5. According to [43,47], (LSE) was determined using Equation (11) after the PV calculation:

$$LSE = 0.004 \times 1.896(P_v) + 0.986 \quad (11)$$

$$LSE = 0.004 \times PV + 0.986 \quad (12)$$

Stage 6. According to [43,47], LST was determined in degrees Celsius for bands 10 and 11 using Equations (12) and (13):

$$LST = \frac{BT}{\{1 + [\lambda BT/\rho]\ln(LSE)\}} \quad (13)$$

where λ is the wavelength of the emitted radiance, and ρ was calculated as (Equation (12))

$$TB = h\frac{c}{\sigma} = 1.438 \times 10^{-2}\ mk \quad (14)$$

According to [42,43], the Boltzmann constant (σ) is 1.38×10^{-23} J/K, Planck's constant (ih i) is 6.626×10^{-34} J s, and light velocity (c) is 2.998×10^{8} m. Stage 7: Using cell statistics in ArcGIS V10.5 software, Equation (13) generated the final Landsat 8 LST by averaging the band 10 and band 11 LST.

2.5. Calculation of Seasonal UHI and UTFVI

To assess a region's municipal fitness and climatic attributes, we do not compare images within the identical year, since weather conditions may differ. A standardized technique was utilized to depict UHI situations in various phases of one year using Equation (14) [48]:

$$UHI = \frac{T_s - T_m}{SD} \quad (15)$$

Ts is the LST, Tm is the research area's LST indicator, and SD is the average. We used UTFVI to express UHI. Ref. [1] estimated monthly LST using LST images and average LST values (Equation (15)). The calculated UTFVI values were categorized on a scale from mild to moderate to profound to highest to characterize urbanization well-being and thermal dispersion in the geographical area [49].

$$UTFVI = \frac{T_s - T_m}{T_s} \quad (16)$$

2.6. Estimating Process of LULC Maps

The CA model-based MOLUSCE plugin in the free and open source QGIS 3.1 projected upcoming LULC alterations. The CA model effectively forecasts LULC transformation, both static and dynamic, and is widely used by researchers [49–52].

2.6.1. Estimating in MOLUSCE Plugin

Using well-known methods like Cellular Automata (CA), Artificial Neural Networks (ANNs), Multi-Criteria Evaluation (MCE), and Weights of Evidence (WoE), MOLUSCE is built to assess, approach, and predict alterations to (LULC). The entry section, area shift evaluation, modeling approach, simulation, and validation are all part of MOLUSCE's intuitive design, which guides users through various processes.

To forecast LULC transitions, the CA-ANN model in the MOLUSCE plugin required the definition of specific spatial transition drivers, simulation settings, and constraints. In this study, LULC class transitions served as the dependent variable. The spatial transition drivers (independent variables) utilized to evaluate the suitability of land conversion included the altitude gradient (derived from the DEM), distance to major highways, and proximity to major shopping districts and urban centers. The model calibration strategy relied on area change analysis using the historical LULC maps from 1993, 2003, 2013, and 2023 to compute the historical transition matrices and empirical transition probabilities. The ANN algorithm was trained using these historical drivers, with a maximum of 1000 iteration trials to establish the complex, non-linear relationships between the LULC changes and the spatial drivers. For the Cellular Automata (CA) simulation settings, a standard 3 × 3 cell neighborhood (nine adjacent cells) was defined to determine the localized probability of land cover transitions based on the state of neighboring pixels. No absolute spatial constraints (such as protected ecological zones or major water bodies) were applied in the model, as the barren land in the study area is widely convertible. The resulting simulated maps for 2033 and 2043 were generated by the computational phase, together with confidence functions (testing) and probable transition maps. The CA modeling method was used to construct these simulated LULC maps. Using kappa statistics including % accuracy and standard kappa, we assessed the predicted LULC maps for accuracy throughout the validation phase. Furthermore, the IDRISI Selva program was used to compute the kappa statistic, which was then used to boost the accuracy of the forecast maps.

2.6.2. Evaluation of the Seasonal LST and UTFVI Processes

The FFNN, RBFNN, RNN, CNN, and MNN are six of the most used neural network algorithms. With the use of machine learning, we can forecast the LST and UTFVI futures for 2033 and 2043, respectively; five algorithms were employed using Q.GIS software: (ANN), (ResNet), and GEE. These algorithms are extensively utilized in image processing and prediction studies, as demonstrated by the research of [50,51,53,54].

2.6.3. Evaluating the Efficiency of the Models

Two statistical matrices, RMSE and R, were evaluated for algorithm efficiency assessment by contrasting projected and measured LST for the year 2023, as specified in Equations (16) and (17).

$$\mathrm{RMSE} = \sqrt{\frac{\sum[\mathrm{T_{obs}} - \mathrm{T_{model}}]^2}{\mathrm{n}}} \tag{17}$$

$$\mathrm{R} = \frac{\sum(\mathrm{T_{obs}} - \mathrm{T_{obs}})\,(\mathrm{T_{model}} - \mathrm{T_{model}})}{\sqrt{\sum(\mathrm{T_{obs}} - \mathrm{T_{obs}})^2(\mathrm{T_{model}} - \mathrm{T_{model}})^2}} \tag{18}$$

According to [55], RMSE and the root–absolute ratio are the most used geography model efficiency measures. With RMSE near 0, efficiency is optimal. A strong correlation (R = 1) substantially links the variables. The R = −1 correlation suggests otherwise. ANN's RMSE and R values were 0.53 and 0.87, surpassing AlexNet's 0.69 and 0.81. From algorithm efficiency, ANN estimated seasonal LST and UTFVI. Environmental use cases favor MLP feed-forward ANNs [55], as described in the following section (Sections 2.6.1–2.6.3).

2.6.4. ANN Forecasting Algorithm

In order to prepare the research geographical area for running the ANN model, sample points were generated using QGIS software, and the area was partitioned into a 600 m × 600 m horizontal grid.

According to [56], this grid size was chosen because it is the smallest area where a single point feature may have a substantial influence on LST and geothermal variation. Furthermore, to balance computational efficiency with spatial fidelity, we effectively capture continuous neighborhood-level patterns while smoothing out micro-scale "salt-and-pepper" anomalies. The number of hidden neurons was evaluated between 5 and 20, with 10 selected as the ideal threshold to maximize accuracy while preventing overfitting. We tested learning rates from 0.01 to 0.20, ultimately adopting 0.10 to achieve efficient and stable convergence. To minimize oscillations during weight updates and maintain training stability, a momentum factor of 0.05 was chosen from a tested range of 0.01 to 0.10. The maximum number of iterations was set to 1000 (tested between 500 and 1250) because model errors plateaued around 850 iterations. For the dataset, a 70:30 training-to-validation split was selected from a 60:40 to 80:20 testing range, offering the best balance between model generalization and learning capacity. Finally, the Sigmoid activation function was favored over ReLU and Tanh due to its stable handling of nonlinear relationships, and Mean Squared Error (MSE) was utilized as the loss function to ensure consistent predictions across continuous environmental variables. The input parameters for the ANN model comprised the average values of the LST and ecological variation pixels inside these 600 m square spatial units, as well as the main dimensions (longitude and latitude) computed in QGIS. Among inputs to the ANN model, we provided a series of p-year LST data, LULC maps, NDBI pictures, and latitudes and longitudes at 10- and 20-year intervals for seasonal LST predictions. According to [57,58], this input was made to find similarities in the database so that predictions could be made using the time series data. With the same method, we were able to forecast seasonal geothermal variation using latitude, longitude, NDBI, LULC, and UHI data collected at 10- and 20-year intervals. These equations mathematically reflect the expected seasonal LST and UTFVI outputs for the next ten (t + 10) and twenty (t + 20) years, respectively, as shown in Equations (18)–(21).

$$\mathrm{LST}(t+10) = f[\mathrm{LST}(t), \mathrm{LST}(-10), \mathrm{LULC}(t), \mathrm{LULC}(-10), \mathrm{NDBI}(t), \mathrm{NDBI}(t-10)] \quad (19)$$

where t = 2023

$$\mathrm{TB} = \mathrm{LST}(t+20) = f[\mathrm{LST}(t), \mathrm{LST}(t-20), \mathrm{LULC}(t), \mathrm{LULC}(t-20), \mathrm{NDBI}(t), \mathrm{NDBI}(t-20)] \quad (20)$$

where t = 2023

$$\mathrm{UTFVI}(t+10) = f[\mathrm{LST}(t), \mathrm{LST}(t-10), \mathrm{UHI}(t), \mathrm{UHI}(t-10), \mathrm{LULC}(t), \mathrm{LULC}(t-10), \mathrm{NDBI}(t), \mathrm{NDBI}(t-10)] \quad (21)$$

where t = 2023

$$\mathrm{UTFVI}(t+20) = f[\mathrm{LST}(t), \mathrm{LST}(t-20), \mathrm{UHI}(t), \mathrm{UHI}(t-20), \mathrm{LULC}(t), \mathrm{LULC}(t-20), \mathrm{NDBI}(t), \mathrm{NDBI}(t-20)] \quad (22)$$

where t = 2023.

2.6.5. Determining the Quantity of Secret Layers and Connections

Because a system can only display nonlinear dynamics with a certain number of invisible layers and cells, these parameters have a profound influence on the outcomes of simulations [56,58]. The algorithm's ability to analyze datasets is improved with higher levels of concealment and connections and generate accurate predictions [58]. Following several experiments, we configured six hidden layers for seasonal LST forecasting and seven hidden layers for UTFVI forecasting (Figures 2–4). Each layer contained 1–3n hidden

neurons, where 3 corresponds to the time series layers at 10-year intervals, and n is 7 for LST and 10 for UTFVI, based on the input layers specified in Equations (18)–(21).

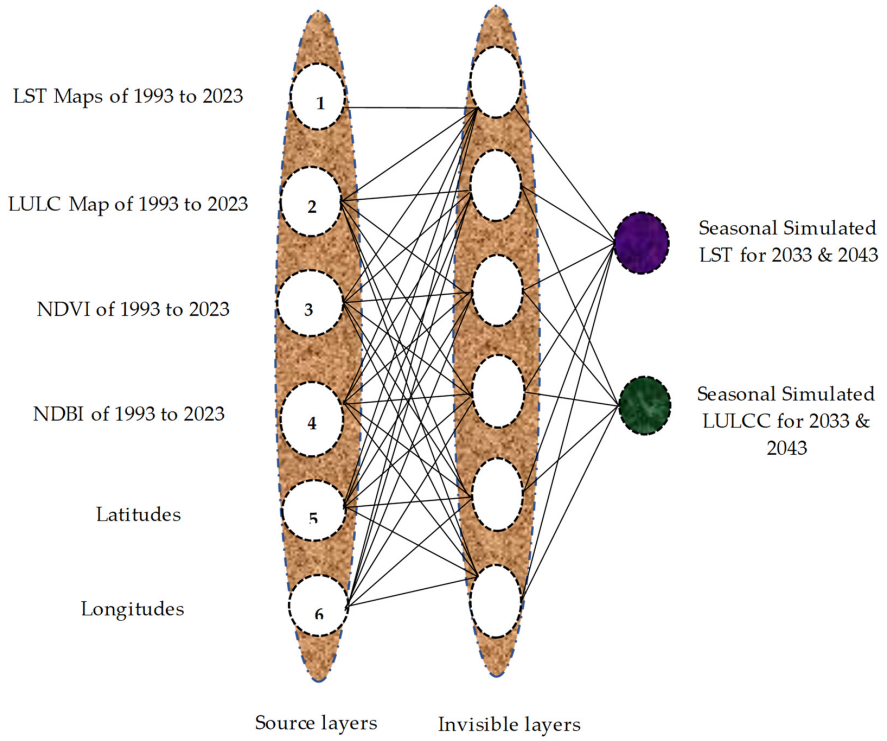


Figure 2. Structural framework for a three-layer ANN approach for predicting seasonal LST and LULCC.

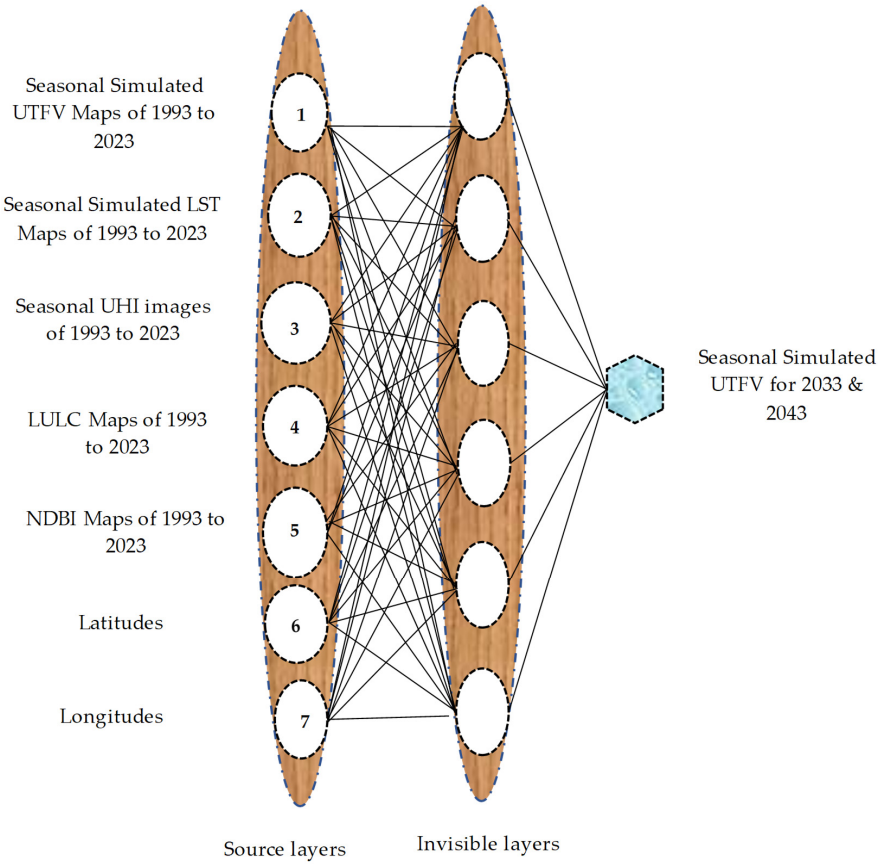


Figure 3. Dynamic UTFVI forecasting with a three-layer ANN model.

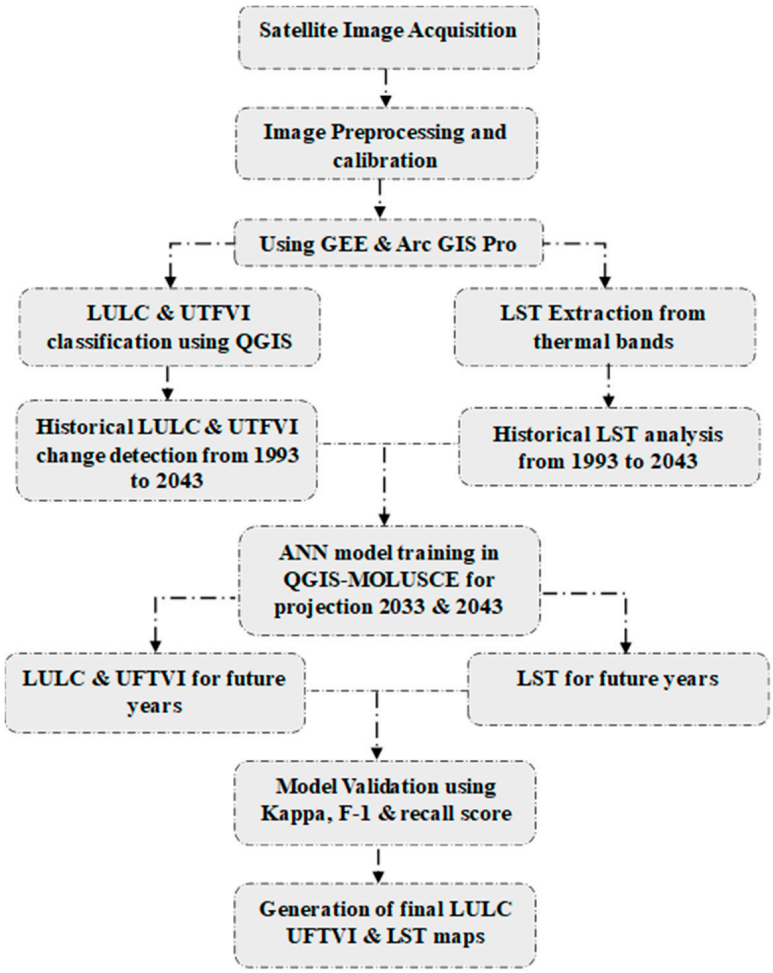


Figure 4. Flowchart illustrating the LULC and LST map predication process using machine learning techniques in QGIS.

3. Results

3.1. Accuracy Assessment

The study employed (GEE) to analyze complex land use changes over the past three decades, from 1993 to 2023. To assess the accuracy of land use classifications, several metrics were utilized, such as the κ factor, general precision, consumer precision, and production consistency. For completeness' sake, we added other evaluation criteria to kappa, even though it has reliably produced correct equity analysis findings. The agreement between the presented and observable surface area classifications was measured using overall kappa statistics. The kappa coefficients were as follows: 86.2% in 1993, 88.1% in 2003, 89.3% in 2013, and 87.1% in 2023. These coefficients indicate a high level of agreement across the study period, with slight variations reflecting changes in land use patterns and classification accuracy. The land use maps for Riyadh demonstrated the following overall accuracy rates: 85.2% in 1993, 84.2% in 2003, 85.7% in 2013 and 83.4% in 2023. These accuracy rates, detailed in Table 4, show a consistently high level of classification accuracy throughout the study period, despite minor fluctuations. The slight decrease in the overall accuracy in 2023 may be attributed to more complex land use patterns or changes in classification methodology. The GEE-based analysis provided robust and reliable land use classifications for Riyadh over the past three decades, as evidenced by the high kappa coefficients and overall accuracy rates.

Table 4. Evaluation of the image's precision.

	User Accuracy (%)			Producer Accuracy (%)				
Year	Vegetation	Barren Land	Built-Up	Vegetation	Barren Land	Built-Up	Overall Accuracy	Kappa Statistics
1993	0.86	0.88	0.85	0.89	0.89	0.85	0.852	0.862
2003	0.88	0.86	0.88	0.88	0.86	0.80	0.842	0.881
2013	0.88	0.87	0.89	0.85	0.85	089	0.857	0.893
2023	0.86	0.88	0.88	0.88	0.89	0.85	0.834	0.871

To evaluate the performance of our machine learning model, we examined precision, recall, and the F1-score after training all classifiers. These metrics are crucial for assessing the quality and predictive capability of the model. Table 5 presents the accuracy, macro average, and weighted average of land use classifications in Riyadh for the years 1993, 2003, 2013, and 2023. The precision, recall, and F1-score accuracy for each year were reported as follows: 1993: 83.2%, 2003: 85.8%, 2013: 85.2%, and 2023: 86.1%. The weighted averages for these key metrics varied over the years: 1993: precision: 83.2%, recall: 85.2%, F1-score: 86.5%; 2003: precision: 85.8%, recall: 85.8%, F1-score: 87.8%; 2013: precision: 89.7%, recall: 86.2%, F1-score: 85.1%; 2023: precision: 85.9%, recall: 90.9%, F1-score: 88.9%. These results indicate a generally high and consistent performance of the machine learning model in classifying land use in Riyadh over the past three decades. The highest precision, recall, and F1-score were observed in 2003, reflecting a particularly strong model performance during that year. Although there were minor fluctuations in these metrics across different years, the overall performance remained robust, demonstrating the reliability and effectiveness of the machine learning approach in land.

Table 5. Model evaluation metrics for the classified imageries.

Year	Parameter	Vegetation	Barren Land	Built-Up	Accuracy	Macro Avg	Weighted Avg
1993	Precision	0.860	0.880	0.893	0.832	0.858	0.867
	Recall	0.873	0.880	0.875	0.852	0.870	0.852
	F1-score	0.899	0.867	0.883	0.862	0.840	0.881
2003	Precision	0.880	0.844	0.870	0.858	0.891	0.859
	Recall	0.846	0.880	0.858	0.858	0.883	0.858
	F1-score	0.872	0.871	0.899	0.878	0.845	0.857
2013	Precision	0.890	0.860	0.883	0.892	0.858	0.857
	Recall	0.833	0.860	0.875	0.832	0.827	0.832
	F1-score	0.889	0.847	0.903	0.862	0.840	0.871
2023	Precision	0.878	0.880	0.984	0.859	0.861	0.864
	Recall	0.878	0.886	0.863	0.909	0.857	0.869
	F1-score	0.878	0.880	0.880	0.889	0.857	0.859

3.2. Monitoring LULC Transitions

An assessment of (Tables 6, 7 and A1 and Figure 5) reveals the substantial amount of surface area changes in Riyadh city over the last three decades. The data indicate notable trends in the expansion of built-up areas: the developed or built-up areas in Riyadh have expanded significantly. In 1993, these areas made up 13.5% of the city's land cover. By 2023, this figure had grown to 19.5%, representing a 44.4% increase over three

decades. This expansion reflects the city's rapid urbanization driven by population growth and economic development. While essential for accommodating a growing population and boosting the economy, this increase in built-up areas often leads to reduced green spaces and natural landscapes, with potential adverse effects on the environment, such as increased pollution and urban heat island effects. Shifts in vegetation and barren land: In 1993, vegetation covered 0.771% of Riyadh's land, and barren land constituted 88.31%. By 2023, vegetation had decreased to 0.67%, corresponding to a 13% reduction, while barren land had reduced to 79.61%. These changes indicate a slight decrease in vegetation and a more pronounced reduction in barren land, suggesting that substantial portions of the formerly undeveloped region have been transformed into developed areas. The reduction in vegetation is concerning as it implies a loss of natural green spaces essential for carbon sequestration, cooling urban areas, and providing recreational areas for residents [59].

Table 6. Area (km^2) along the study area periods.

LULC	Built-Up	Vegetation	Barren Land	Total
	km^2	km^2	km^2	km^2
1993	646.64	46.04	5277.03	5969.71
2003	806.69	40.19	5122.82	5969.7
2013	899.49	66.74	5003.45	5969.7
2023	1168.26	40.28	4760.75	5969.71

Table 7. Area (%) along the study area periods.

LULC	Built-Up (%)	Vegetation (%)	Barren Land (%)
1993	10.83	0.771	88.31
2003	13.51	0.673	85.75
2013	15.06	1.117	83.73
2023	19.56	0.674	79.61

On the other hand, in 2023, vegetation still increased and covered 40.28 km^2 (1.4%). But the decline in vegetation, from 2033 to 2043, will increase from 36.48 km^2 to 40.23 km^2 (0.611 to 0.688) further exacerbating the challenges posed by urbanization. Vegetation, crucial for reducing air pollution, providing shade, and enhancing visual appeal, is rapidly disappearing in Riyadh. These changes raise concerns about the sustainability of Riyadh's urban environment and its impact on local ecosystems and residents. Deforestation negatively impacts the ecological functioning, aesthetic value, and biodiversity of the region. Build-up area in Riyadh, are widespread in rapidly growing cities across Saudi Arabia.

These patterns underscore the urgent need for implementing sustainable urban development strategies. Riyadh must prioritize the establishment of efficient ecological strategies to accommodate its expanding cities without depleting natural resources. This involves integrating green infrastructure into urban expansion plans and restoring damaged ecosystems. Sustainable development principles should guide urban expansion to ensure that environmental health is not compromised for social and economic progress [60]. Developing resilient and sustainable solutions requires a multifaceted approach involving government policies, community engagement, and scientific research. Addressing the challenge of Riyadh's expanding urban areas and diminishing natural habitats requires coordinated, long-term efforts. Without intervention, the functional and aesthetic integrity of the Riyadh landscape is at risk, threatening the region's long-term viability. To overcome these chal-

lenges and ensure sustainable growth while preserving its natural heritage, conservation initiatives, sustainable urban design, and community involvement are essential [61].

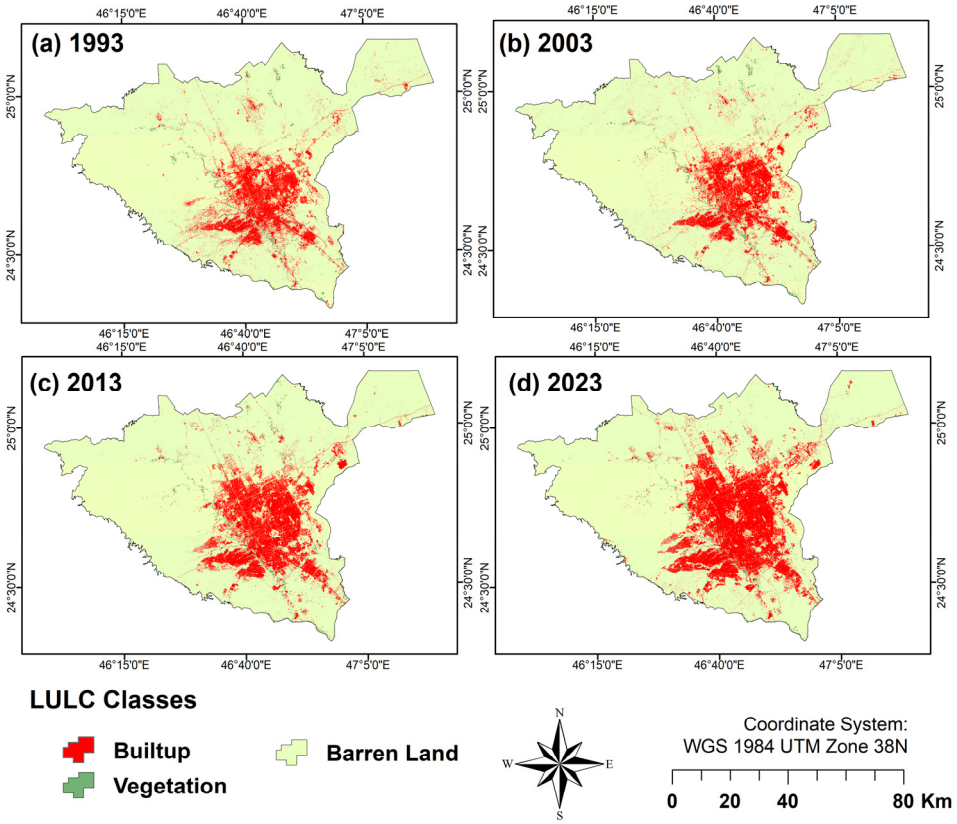


Figure 5. Land use classes in Riyadh in (**a**) 1993, (**b**) 2003, (**c**) 2013, and (**d**) 2023.

Over the last thirty years, swift construction has become the predominant force behind extensive changes in land use in the Riyadh region, as illustrated in Table 8. The built-up areas have more than doubled, increasing from 268.77 km^2 in 2013–2023 to 520.477 km^2 in 1993 to 2023, and barren land from 2013 to 2023 decreased by 246.42 km^2, marking the most prominent transformation, which will increase to −181.24 km^2 in (2023–2033). This substantial expansion reflects the region's urban development, placing significant pressure on land resources already strained by the demands of a growing population and urban infrastructure.

Table 8. LULCC area (km^2) transition across the study area periods from (1993 to 2043).

Class	1993–2003	2003–2013	2013–2023	2023–2033	2033–2043
Built-up	160.05	92.8	268.77	187.62	1.586
Vegetation	−5.85	26.55	−26.46	−3.8	153.527
Barren land	−152.92	−120.05	−246.42	−181.24	3.757

3.3. Change in Summer and Winter LST

The conversion process of land cover in Riyadh has highlighted significant fluctuations in surface temperatures across the area over the past three decades. Tables 9 and 10 and Figures 6, 7 and A1 provide detailed illustrations of the seasonal LST ranges from 1993 to 2023, revealing noticeable upward trends in temperature in both urban and municipal areas of Riyadh. The data indicate a substantial rise in the highest average summer temperatures recorded in urban areas of Riyadh. In 1993, the highest average temperature during

summer was 56.73 °C. By 2003, this temperature had increased to 58.25 °C. This trend continued, with the highest summer temperature further rising from 58.87 °C to 59.89 °C by 2023. These increments represent a significant upward shift, suggesting that the urban areas of Riyadh are experiencing increasingly hotter summers over the years [62]. Similar warming trends have been reported in other arid and semi-arid cities worldwide. Studies in Middle Eastern cities such as Baghdad, Erbil, and Amman have documented significant increases in land surface temperature linked to rapid urban expansion and vegetation loss [63]. Likewise, research in Jaipur, India, reported a rise in summer LST from about 46.9 °C in 1993 to 56.5 °C in 2020 [64]. These findings indicate that the increasing summer temperatures observed in Riyadh are consistent with patterns reported in other arid and semi-arid urban regions [65].

Table 9. Comparison of seasonal summer LST of Riyadh from 1993 to 2023 (Q1 → 25th percentile, median (Q2) → 50th percentile, Q3 → 75th percentile).

Year	Summer					
	Min (°C)	Q1	Median	Q3	Max (°C)	Mean (°C)
1993	23.28	33.05	40.50	49.50	56.7307	40.05
2003	24.20	34.57	41.22	50.23	58.25	41.22
2013	29.02	35.49	43.94	52.89	58.87	43.94
2023	28.27	36.88	44.08	53.66	59.89	44.08

Table 10. Comparison of seasonal winter LST of Riyadh from 1993 to 2023, (Q1 → 25th percentile, median (Q2) → 50th percentile, Q3 → 75th percentile).

Year	Winter					
	Min (°C)	Q1	Median	Q3	Max (°C)	Mean (°C)
1993	13.32	18.91	22.35	26.57	30.75	22.35
2003	13.44	18.70	22.63	25.94	29.16	22.63
2013	14.65	19.45	23.35	26.93	31.62	23.35
2023	16.64	20.73	24.48	28.06	32.33	24.48

The rising temperatures in summer can be attributed to several factors associated with urbanization, such as the reduction in green spaces, increased built-up areas, and the proliferation of heat-absorbing surfaces like concrete and asphalt. These surfaces retain heat during the day and release it slowly at night, contributing to the urban thermal flux heterogeneity effect, which exacerbates the overall temperature rise in urban areas. Similarly, the highest winter temperatures in Riyadh have shown an upward trend. In 1993, the highest recorded temperature in winter was 30.75 °C, which increased to 32.33 °C by 2023. When analyzed in percentage terms, summer temperatures increased by approximately 2.6% between 1993 and 2003, while winter temperatures increased by 5.1% during the same period, indicating that the relative rise in winter temperatures is actually more pronounced than in summer. Although the absolute change in winter temperatures is smaller than that of summer, the proportional increase highlights that Riyadh's climate is warming year-round. This persistent warming during winter can reduce seasonal relief, altering energy demand patterns and increasing the need for cooling even during traditionally cooler months.

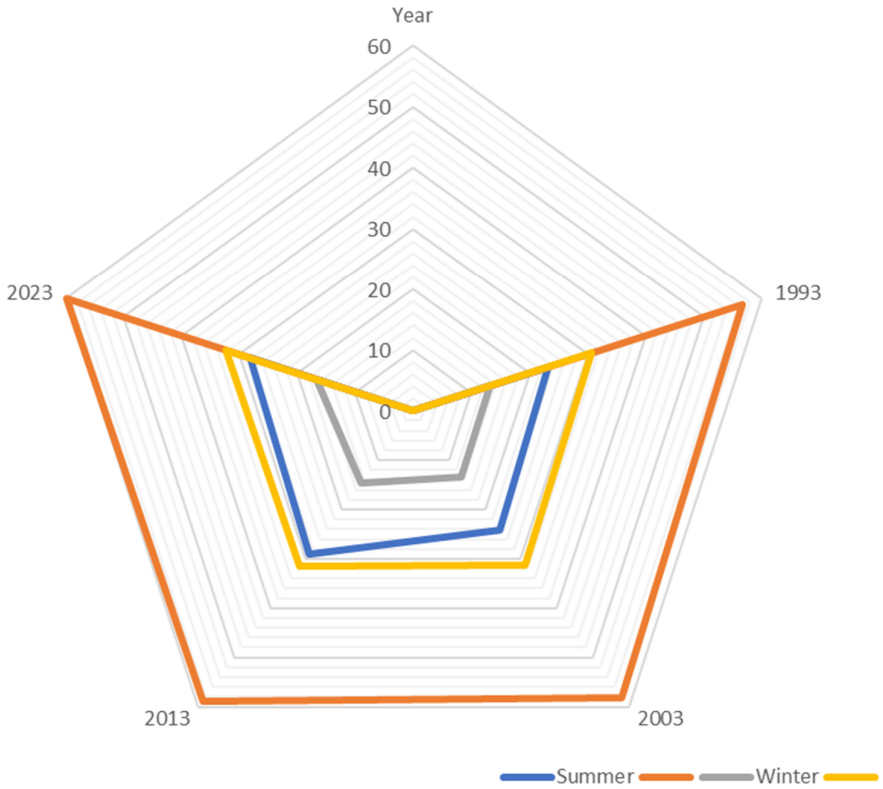


Figure 6. Riyadh's LST (spider diagram) in the winter and summer from 1993 to 2023.

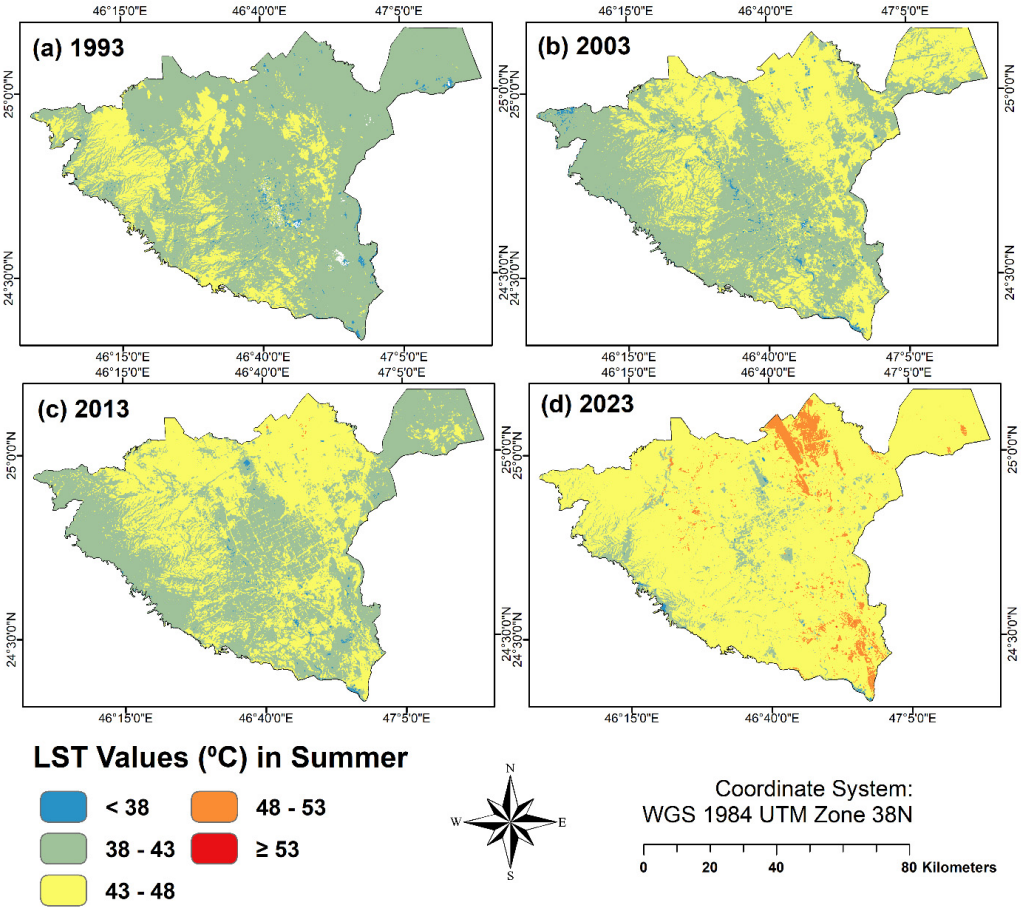


Figure 7. LST map of summer season in (**a**) 1993, (**b**) 2003, (**c**) 2013, and (**d**) 2023.

A detailed analysis of Figures 7 and A2, Tables 11 and A2 reveals that summer temperature variations in Riyadh have exhibited significant changes over the past three decades. The data highlight a noticeable increase in temperature ranges and the extent of areas affected by higher temperatures. For the temperature distribution in 1993, approximately 92% of Riyadh city experienced summer temperatures ranging between 38 °C and 43 °C. This indicates that nearly the entire city was within this relatively moderate temperature range during the summer months. Shifts observed in 2003 and 2013: By 2003, the proportion of the city with temperatures between 38 °C and 43 °C had decreased to about 55.80%.

Table 11. Area's range-wise LST distribution, 1993 to 2043.

Year	Summer Season LST Range in °C									
	<38		38–<43		43–<48		48–<53		≥53	
	Area (km^2)									
1993	380.29	6.37	5506.52	92.24	82.683	1.385	0.08	0.0013	0.01	0.0002
2003	52.32	0.87	3331.17	55.80	2585.2	43.309	0.56	0.0093	0.03	0.0011
2013	24.92	0.41	3143.18	52.65	2799.0	46.88	2.49	0.041	0.04	0.0074
2023	12.34	0.20	398.26	6.67	5225.2	87.529	333.6	5.589	0.196	0.0032
2033	9.93	0.16	242.16	4.05	4583.7	76.784	1131	18.955	2.202	0.0369
2043	8.10	0.13	162.92	2.72	3429.7	57.401	2348	39.305	20.39	0.341

Additionally, the data show an emerging trend where 43.30% of the area experienced higher temperatures, ranging from 43.2 °C to 48 °C. This shift indicates a significant increase in the areas affected by higher temperatures within a decade. Continuing this trend, the year 2013 saw further changes. Only 52.65% of the city had temperatures in the 38 °C to 43 °C range, showing a reduction compared to 1993. Meanwhile, areas with temperatures between 43.2 °C and 48 °C increased to 46.88%.

These data suggest that nearly half of the city's area had transitioned to experiencing higher temperatures. It significant increased by 2023, and the most dramatic changes are observed by 2023. While, in 1993, only 1.38% of the city had summer temperatures between 43 °C and 48 °C, this figure rose substantially over the next two decades. By 2023, around 87.52% of Riyadh's area was experiencing temperatures within this higher range. This substantial increase indicates a significant shift in the summer temperature profile of the city.

An analysis of Riyadh's summertime variations in temperature between 1993 and 2023 indicates a notable and alarming pattern of rising levels and growing blasting zones. This pattern emphasizes how urgently thorough strategies are needed to lessen the effects of these changes. Comprehensive public health programs, efficient climate adaption strategies, and innovative urban planning are necessary to handle the problems brought on by increasing temperatures and to improve the resilience and health of Riyadh's citizens [66].

As shown in Figures 8 and A2 and Table 12, a comprehensive analysis of winter season temperatures in Riyadh reveals significant shifts in temperature ranges over the past three decades, with predictions indicating continued trends into the future. This analysis draws on data from 1993, 2003, 2013, and 2023, and extends to predictions for 2033 and 2043. During the winter season, temperatures in Riyadh typically range between 15 °C and 25 °C. In 1993, 77.78% of Riyadh experienced temperatures between 15 and 20 °C, while 21.25% experienced temperatures between 20 °C and 25 °C. By 2003, about 85.28% of the area had temperatures in the 15 °C to 20 °C range. However, by 2013, this percentage had decreased to 64.69%. This trend continued into 2023, where approximately

79.88% of the city experienced temperatures between 20 °C and 25 °C, indicating a gradual increase in temperatures over the years. Looking ahead to 2033 and 2043, predictions suggest that around 92.70% of Riyadh will experience temperatures between 20 °C and 25 °C, with this figure decreasing to about 35% by 2043, indicating a potential slight reduction in this temperature range. The analysis of winter temperature variations in Riyadh from 1993 to 2023, along with projections for 2033 and 2043, reveals a clear trend of increasing temperatures. This shift underscores the ongoing impact of climate change and urbanization on local climates.

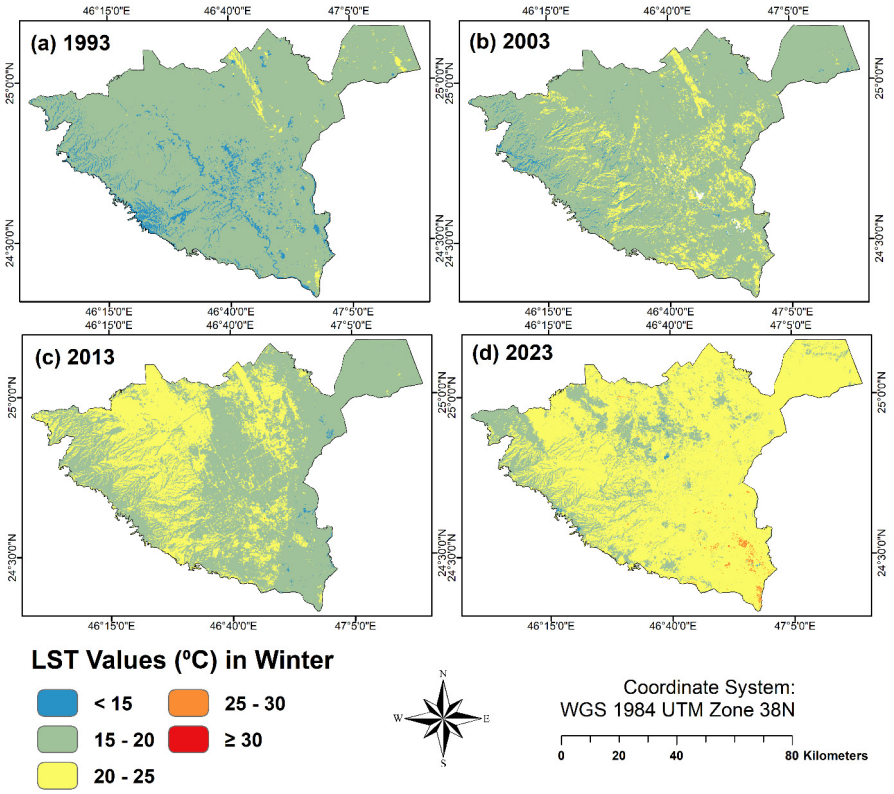


Figure 8. LST map of winter season in (**a**) 1993, (**b**) 2003, (**c**) 2013, and (**d**) 2023.

Table 12. Winter season LST varies in 1993 to 2043.

Year	Winter Season LST Range in °C									
	<15		15–<20		20–<25		25–<30		≥30	
	Area (km^2)									
1993	57.06	0.955	4643.22	77.78	1268.59	21.25	0.15	0.002	0.05	0.0008
2003	100.64	1.685	5091.53	85.28	777.34305	13.02	0.34	0.005	0.04	0.0006
2013	19.7	0.33	3879.77	64.99	2069.52	34.66	0.16	0.002	0.05	0.0008
2023	14.43	0.241	1149.41	19.25	4768.5	79.88	37.05	0.62	0.09	0.0016
2033	11.69	0.195	259.48	4.34	5502.48	92.17	195.76	3.27	0.34	0.005
2043	7.1	0.118	144.11	2.41	5035.29	84.35	780.69	13.07	2.3	0.03

The findings presented in Figure A3 indicate a consistent increase in temperatures in municipal areas from 1993 to 2023. This trend underscores the influence of urbanization on the regional climate, as populated areas tend to exhibit higher LST values compared to less industrialized regions. This phenomenon, known as the thermal flux effect, results from factors such as reduced vegetation, extensive concrete and asphalt coverage, and

human-induced heat sources. Rising temperatures pose challenges to public health and city planning, including increased heat-related health issues, elevated energy demands for cooling, and negative impacts on urban environments. Addressing these challenges requires adaptable strategies to mitigate downtown heat. Potential measures include increasing urban vegetation, employing reflective building materials, and enhancing urban ventilation.

The significant temperature increases observed in Riyadh's urban areas underscore the pressing need for ecologically sustainable urban development. To enhance the resilience of rapidly expanding cities and reduce vulnerability, efforts must focus on mitigating the thermal flux effect and addressing its underlying causes. The analysis of surface temperature fluctuations in Riyadh from 1993 to 2023 reveals a significant and persistent rise in both summer and winter temperatures. This trend highlights the growing thermal stress in urban areas and underscores the urgent need for adaptive measures to mitigate the impacts of rising temperatures. Sustainable urban planning, effective climate adaptation strategies, and enhanced public awareness are essential to address the challenges posed by the increasing temperatures and to ensure the long-term resilience of Riyadh's urban environment.

3.4. The UTFVI Range Varies According to the Time of 1993 to 2023

Riyadh faces significant challenges related to its rapid urbanization and climatic conditions. The growing UHI effect, combined with the city's arid climate, poses risks to public health, energy consumption, and overall livability. However, these challenges also present opportunities for innovative urban planning and sustainable development. Effective strategies to mitigate the UHI effect include increasing green spaces, enhancing urban vegetation, and implementing reflective and cool roofing materials.

The (UFTVI) essentially represents the different place of the urban ecology, focusing on factors such as the quality of urban areas, the comfort of living conditions, public health, safety, and ecological sustainability. Geothermal variation is divided into five categories to provide a comprehensive assessment: weak, middle, strong, stronger, and strongest. These categories serve as thresholds for evaluating the summer and winter conditions in various parts of the urban area, specifically for the Arman area, over the period from 1993 to 2023. The UFTVI categories are designed to measure and explain the ecological robustness of Riyadh city (illustrated in Figures 9 and 10). By categorizing the urban environment into these five levels, the thermal variation offers a nuanced understanding of how different areas within the city fare in terms of their ecological health and sustainability. Over the three decades from 1993 to 2023, different ranges of UFTBI values have been recorded for Riyadh, offering insights into how the city has evolved ecologically. According to [66], the city's overall environmental health helps to determine areas that require intervention and improvement and recognize zones that can serve as models for sustainable urban living.

From Table 13, it can be observed that, during the summer season of 1993, approximately 45% of the area had UTFVI values close to zero, indicating very weak ecological conditions. In the winter season of the same year, this percentage increased to about 55%, still reflecting very weak environmental conditions. In the middle range, covering an area of 414.29 km^2, the UTFVI values extended to around 1697 km^2. This middle range further increased to 2391.36 km^2, or approximately 40%, in the winter season. Examining the data from 2013, we see a different trend. In the summer of 2013, the area with the lowest geothermal variation values increased significantly to about 2955 km^2, representing 47% of the area. In the same year, the area classified as having the strongest values was about 342 km^2. However, over the past two decades, this area with the strongest values has decreased dramatically. Looking at the geothermal variation data for 2023, the situation shows further changes. The values for 2023 indicate a very low range, covering 2778 km^2,

which is a reduction compared to 1993. In the winter of 2023, the UTFVI values stood at approximately 3018.44 km^2, or around 57%. This indicates that, during the winter season, a significant portion of the area still experiences very weak values. Additionally, in the winter of 2023, the strong values remained at just 0.7% across the board. From this data, we can infer that the values for Riyadh city are generally very low, especially in areas outside the urban center. The velocity is somewhat stronger towards the urban center, where the quality of life is marginally better, and people can live more healthily.

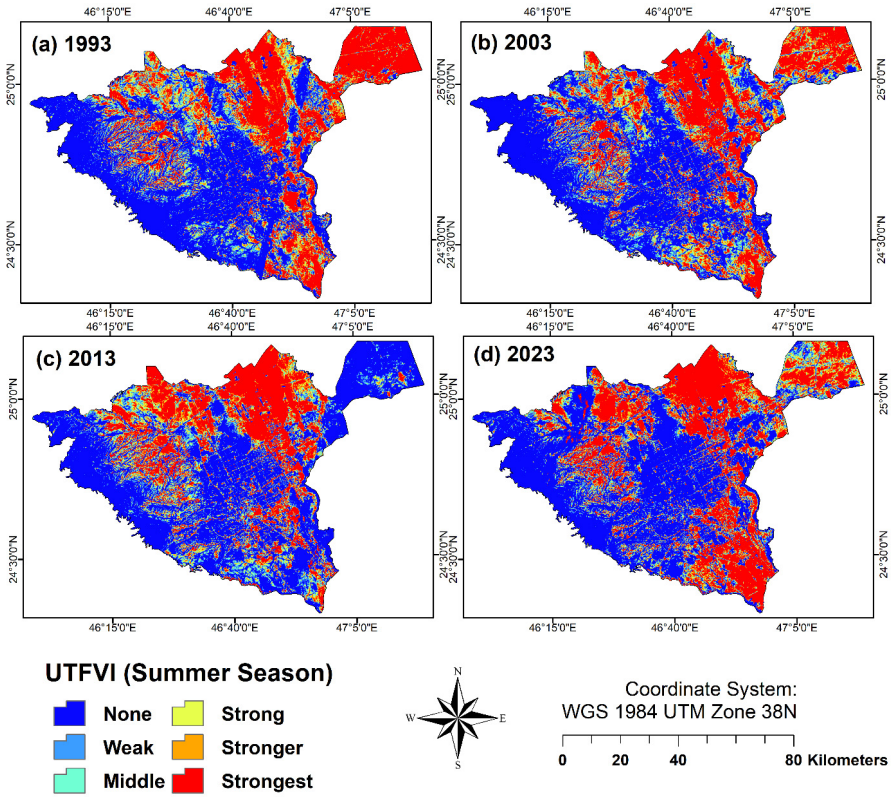


Figure 9. Spatial distribution of summertime UTFVI in (**a**) 1993, (**b**) 2003, (**c**) 2013, and (**d**) 2023.

Table 13. Area (km^2) distribution of seasonal UTFVI in the study area.

	UTFVI	None	Weak	Middle	Strong	Stronger	Strongest
Year	**Ranges**	**<0**	**0–0.005**	**0.005–0.010**	**0.010–0.015**	**0.015–0.020**	**>0.020**
1993	Summer	2670.27	391.163	414.29	413.76	381.93	1697.78
	Winter	3010.5	143.64	136.47	137.44	149.65	2391.36
2003	Summer	2703.25	400.04	437.72	423.63	379.89	1624.8
	Winter	2779.79	193.1	152.51	239.23	160.84	2444.41
2013	Summer	2991.59	415.68	408.38	378.66	342.24	1433.11
	Winter	2761.08	160.39	164.23	170.57	176.48	2536.54
2023	Summer	2778.71	321.8	340.69	354.34	361.74	1812.37
	Winter	3018.44	67.12	67.99	70.167	72.9	2672.56

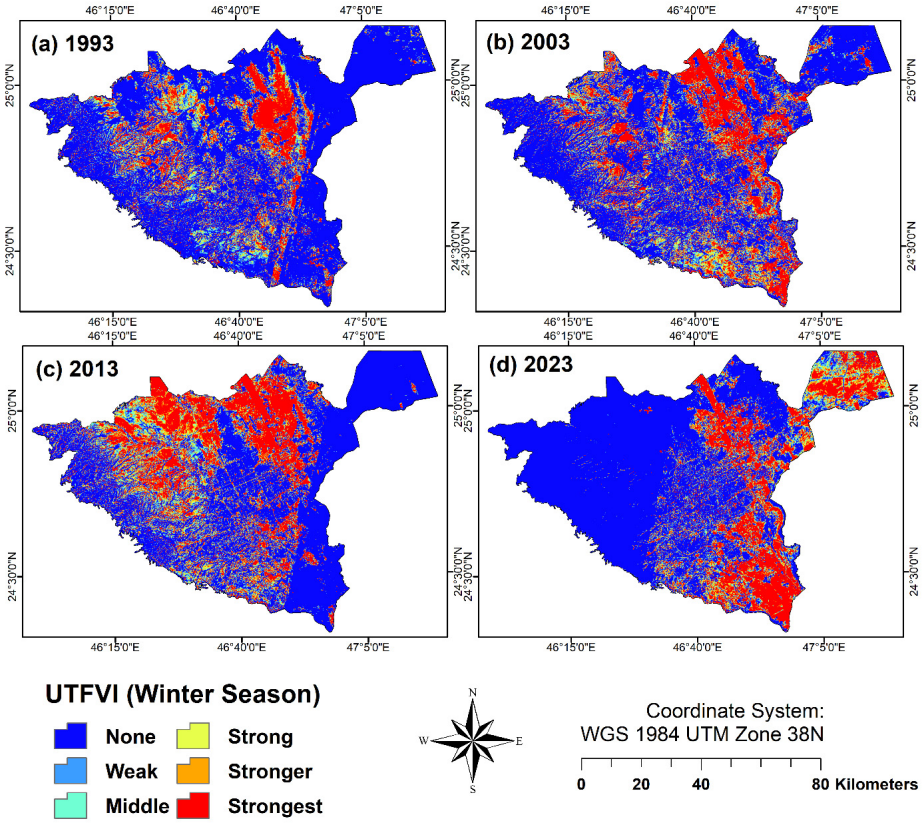


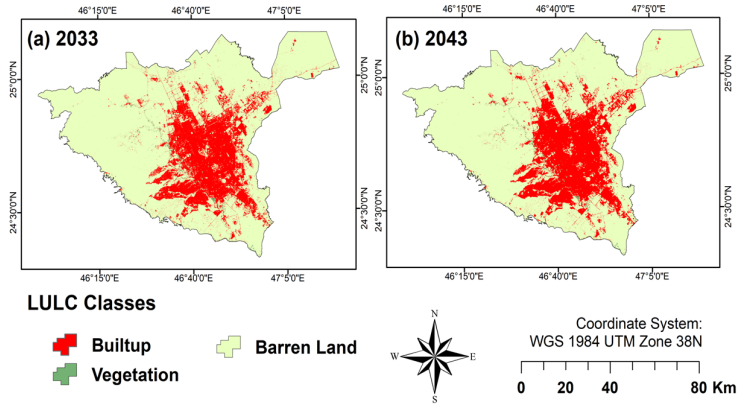
Figure 10. Distribution of winter UTFVI in (**a**) 1993, (**b**) 2003, (**c**) 2013, and (**d**) 2023.

However, the ecological condition in other areas is quite poor, indicating a need for significant environmental improvements to enhance the overall liability and ecological health of the city. The trends observed from 1993 to 2023 show a concerning pattern of weak values spreading across a larger area, particularly during the winter season. This decline in ecological conditions highlights the challenges faced by Riyadh in terms of urban environmental health. The urban center's relatively better UTFVI values suggest that focused efforts on improving urban planning and sustainability could potentially extend these improvements to broader areas, thereby enhancing the ecological balance and quality of life throughout the city. By examining the values across these years, we can track the progress and changes in Riyadh's urban environment. This assessment helps in understanding the impacts of urbanization, climate change, and other factors on the city's ecological health [66]. The categorization into weak, middle, strong, stronger, and strongest provides a clear framework for urban planners and policymakers to prioritize areas for ecological enhancement, ensure the comfort and health of residents, and maintain the city's overall safety and sustainability.

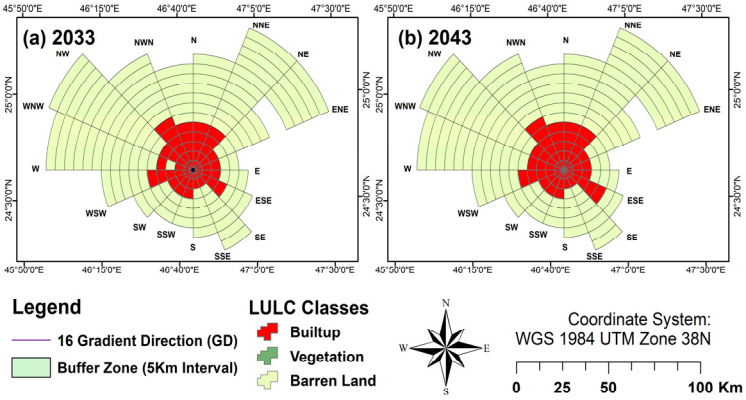
3.5. Forecasting LULC Change

Based on the land use category percentages in 2023, the projections indicate a huge increase in the developed area from 2023 to 2043, as illustrated in Figure 11 and Table 14. This expansion will profoundly affect urban life in Riyadh. The city's area underwent considerable changes between 1993 and 2013, and future predictions from 2033 to 2043 suggest further significant transformations. In particular, expected growth is estimated for the urbanized region, by over 1355.88 km^2, reflecting a 22.7% rise. By 2033, this area is predicted to grow drastically, covering 1509.4 km^2 and marking a 25.28% increase. The period from 2033 to 2043 will see even more substantial urbanization, indicative of broader trends observed in developing world urbanization driven by population growth. However,

this rapid urban expansion will not come without consequences. Alongside the increase in built-up areas, there will be a notable decline in biodiversity. This trend highlights a significant environmental threat, as the increase in urban areas will lead to a decrease in the small amount of preserved vegetation. Additionally, barren land is also expected to experience a reduction.



(I)



(II)

Figure 11. (**I**) LULCC prediction for the years 2023 and 2043 indicated and (**II**) directional changes in the LULC within the study area.

Table 14. Area (km^2) across the study area periods.

LULC	Built-Up		Vegetation		Barren Land		Total
	km^2	%	km^2	%	km^2	%	
2033	1355.88	22.71	36.48	0.611	4577.35	76.57	5969.71
2043	1509.407	25.28	40.237	0.674	4420.05	73.91	5969.70

In 2033, the total land area of Riyadh is projected to consist of 4571.37 km^2 of barren land, accounting for 76.57% of the total area. Vegetation areas will cover approximately 36.48 km^2, making up 0.611% of the total area. By 2043, these proportions are anticipated to shift significantly. Barren land is expected to decrease to 4412.49 km^2, accounting for 73.91% of the total area, while the developed area will swiftly increase to 1509.407 km^2, representing 25.28% of the total area. Vegetative areas are predicted to increase slightly, making up 0.674% of the total area. This substantial urbanization reflects broader trends in urban growth in developing countries, driven by population increases. However, along with the reduction in barren land, this underscores the environmental challenges posed

by rapid urban expansion. The changes in land use categories indicate a pressing need for sustainable urban planning to mitigate the negative impacts on the environment and ensure the sustainability of urban life in Riyadh.

3.6. Validation of Estimated LST

Even with a dependable and well accepted method, the seasonal alteration of LST is limited. A fresh atmosphere and a cloud-free study area are needed for accurate LST measurements. Compared to field data, cloud cover, which was less than 10%, reduced accuracy [67–70]. Considering those variations, it is feasible that the LST dispersion in each and every region is distorted. It can be seen in Table 15 that there were some deviations. In the event that the LST levels were higher than the actual temperatures that were detected by SAMD, the disparity is considered to be a negative deviation (ND), but, if the LST values were lesser, the difference is considered to be positive (PD). In 1993, the maximum LST had the highest positive deviation (PD) (+0.02), while 2023 was the year that it had the foremost ND (+0.04). Furthermore, from 1993 to 2023, the mean PD was found to be (+0.53), whereas the mean ND was found to be (−0.69).

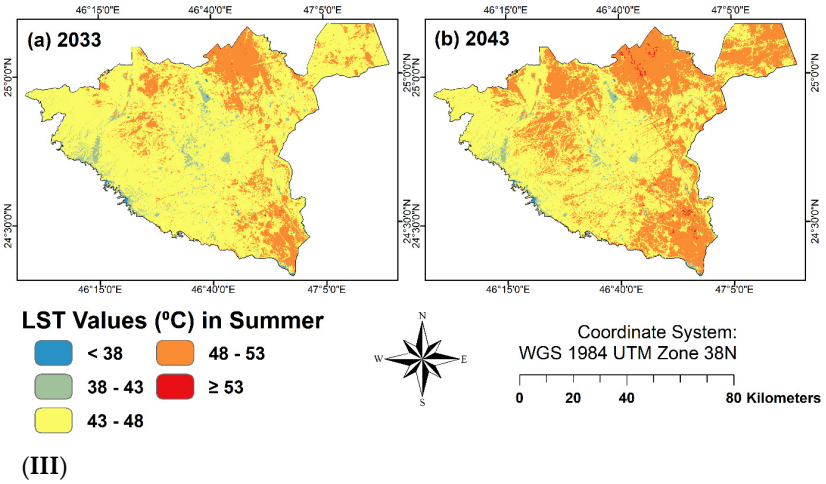
Table 15. Validation of satellite-derived LST with SAMD meteorological station measurements.

Year	Summer								Winter							
	1993		2003		2013		2023		1993		2003		2013		2023	
	Max	Min	Max	Min	Max	Min	Max	Min	Max	Min	Max	Min	Max	Min	Max	Min
LST derived from thermal bands (°C)	56.73	23.28	58.25	24.20	58.87	29.02	59.89	28.27	30.75	13.32	29.16	13.44	31.62	14.65	32.33	16.64
SAMD recorded LST (°C)	56.75	23.35	59.19	24.25	58.90	29.77	60.91	29.55	30.57	12.25	28.16	14.23	32.21	14.16	33.15	16.68
Deviation (°C)	+0.02	+0.07	+0.94	+0.05	+0.03	+0.75	+1.02	+1.28	−0.18	−1.07	−1.00	+0.79	+0.59	−0.49	+0.82	+0.04
Average deviation	+0.05		+0.50		−0.39		+1.15		−0.63		−0.11		+0.05		+0.43	

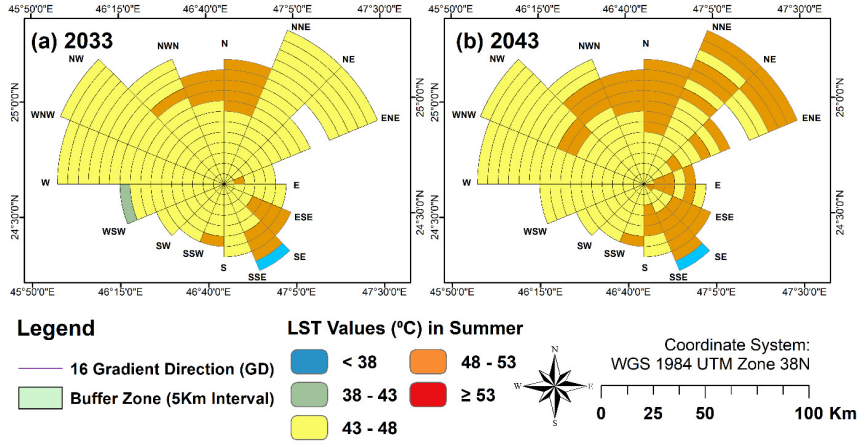
It is evident from the disparities that the LST that was anticipated and the LST that was reported are considerably different. The results are not as trustworthy as they might be owing to the constraints, despite the fact that the RS-derived LST data demonstrated an acceptable correlation with the temperatures that were observed. Because of this quantity of cloud cover, regardless of how little it may be, there is a related degree of uncertainty. Therefore, it is essential to utilize caution while interpreting the LST data that were obtained through RS, and any research that makes use of these data has to be aware of the risk of severe error that is brought about by these limits.

3.7. Forecasting of Seasonal LST

The projections of seasonal LST from 2033 to 2043, as detailed in Figures 12 and 13 and Table 16, reveal substantial upward trends in Riyadh. These trends indicate significant changes in temperature patterns, with notable increases in both summer and winter temperatures. The highest average summer temperature is expected to increase from 60.79 °C in 2033 to 61.52 °C in 2043, marking an increase of approximately 1.08 °C. Such extreme heat will make urban living conditions extremely uncomfortable, exacerbate health issues like heat strokes, damage ecosystems, and undermine sustainable living environments.



(III)



(IV)

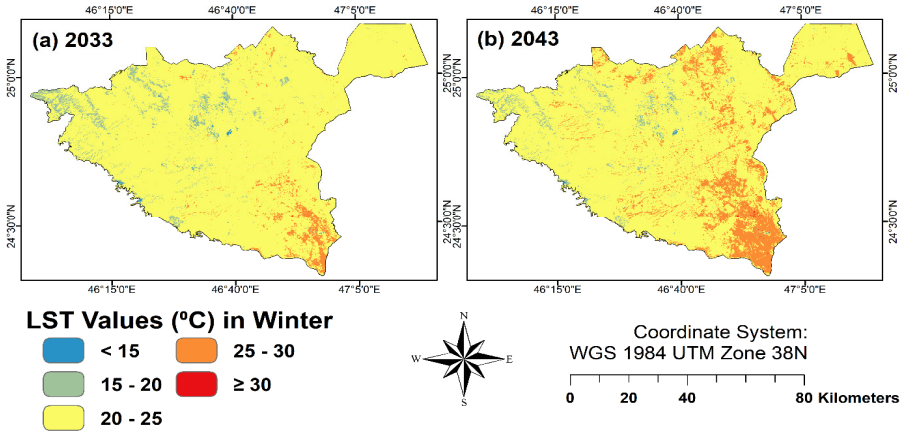
Figure 12. (**III**) Level of temperature change and (**IV**) directional shifts in the LST (summer) in Riyadh from 2033 to 2043.

Table 16. Forecasting LST across the study area periods for 2033 and 2043.

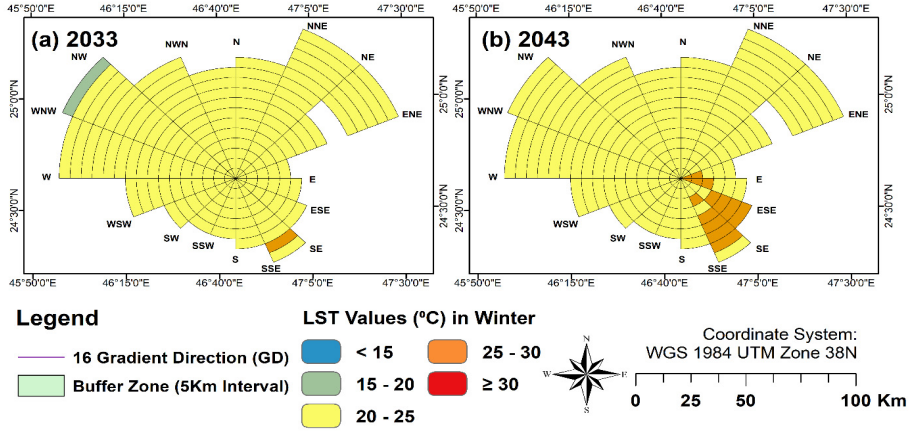
Year	Summer			Winter		
	Min (°C)	Max (°C)	Mean (°C)	Min (°C)	Max (°C)	Mean (°C)
2033	31.14	60.79	45.96	17.54	33.26	25.45
2043	33.12	61.52	47.32	18.98	34.48	26.73

Similarly, the highest average winter temperature is anticipated to rise from 33.26 °C in 2033 to 34.48 °C in 2043, reflecting a 1.22 °C increase. This trend suggests that even traditionally cooler seasons will experience significant temperature rises. The persistence of elevated temperatures indicates substantial thermal stress in urban areas, highlighting the urgent need for measures to mitigate impacts on public health and the environment.

Also, Table 17 presents the predicted temperature trends for both seasons from 2033 to 2039. In the summer of 2033, areas with temperatures of 38 °C or below are projected to cover 9.93 km^2, while areas within the 38 °C to 43 °C range are expected to cover 242.1 km^2. However, areas with temperatures of 53 °C or above are anticipated to sharply decrease to 2.202 km^2.



(**V**)



(**VI**)

Figure 13. (**V**) Level of temperature change and (**VI**) directional shifts in the LST (winter) in Riyadh from 2033 to 2043.

Table 17. LST distributions in the research region that were expected range-wise during both seasons.

Year	Predicted Summer LST range in °C									
	<38		38–<43		43–<48		48–<53		≥53	
	Area (km^2)									
2033	9.93	0.166	242.1	4.055	4583.7	76.78	1131.5	18.95	2.202	0.0006
2043	8.1	0.135	162.9	2.72	3429.7	57.45	2348.52	39.341	20.39	0.0057
	Predicted Winter LST range in °C									
	<15		15–<20		20–<25		25–<30		≥30	
	Area (km^2)									
2033	11.6	0.19	259.48	4.34	5502.4	92.17	195.7	3.27	0.343	0.0057
2043	7.1	0.11	144.11	2.41	5035.2	84.347	780.6	13.07	2.3	0.0385

By 2043, the area covered at 43 °C to 48 °C is predicted to expand to 4583.7 km^2 (76.78%), with areas in the 48 °C to 53 °C range dramatically increasing to approximately 1131.3 km^2. For the winter season in 2033, temperatures of 20 °C to 25 °C or below are forecasted to encompass 92.17 km^2, increasing to nearly 84.34 km^2 in the 20 °C to 25 °C range. However, by 2043, this area is expected to significantly diminish to only 13.07 km^2

in the 20 °C to 25 °C range. The area with temperatures at 30 °C or below is predicted to cover 780.6 km^2, but for temperatures $\geq$ 30 °C, it will rise sharply to 2.3 km^2. These predictions indicate a significant and troubling trend of rising temperatures in Riyadh. The predicted increases in both summer and winter temperatures highlight the potential for exacerbated thermal stress on urban populations, increased health risks, and substantial environmental impacts.

In addition to the correlation coefficient (R), the Root Mean Square Error (RMSE) was used to evaluate the magnitude of prediction errors. The RMSE provides a quantitative measure of the difference between predicted and observed values and allows the assessment of potential bias and amplitude deviations in the model outputs. Given the increasing trends in seasonal LST patterns, predicting future LST is essential to forecast the effects of the (UHI). We used an (ANN) model to predict future seasonal LST ranges. Our estimates for 2023, evaluated using the (RMSE) and the R-squared statistic, were promising. The RMSE value was 0.759 for summer LST, and the R-squared value was 0.93 for summer LST. In addition, the RMSE value was 0.789 for winter LST, and the R-squared value was 0.87 for winter LST. Finally, Table 18 indicates a strong correlation between the predicted and observed results. This agreement validates our ANN-based approach for predicting future LST changes. The predicted LST values indicate a concerning trend of rising temperatures in Riyadh, particularly in regions covering a substantial part of the city. Comprehensive urban planning that emphasizes environmentally friendly activities is crucial to address these challenges. This includes improving eco-friendly infrastructure and creating effective watershed management systems.

Table 18. Validation of the projected seasonal LST for 2023.

Prediction Year	Evaluation of QGIS-Based ANN–CA Models for LST Forecasting		
	No of Hidden Layer	RMSE	R
Summer 2023	6	0.759	0.93
Winter 2023	6	0.789	0.87

3.8. Forecasting of Seasonal UTFVI

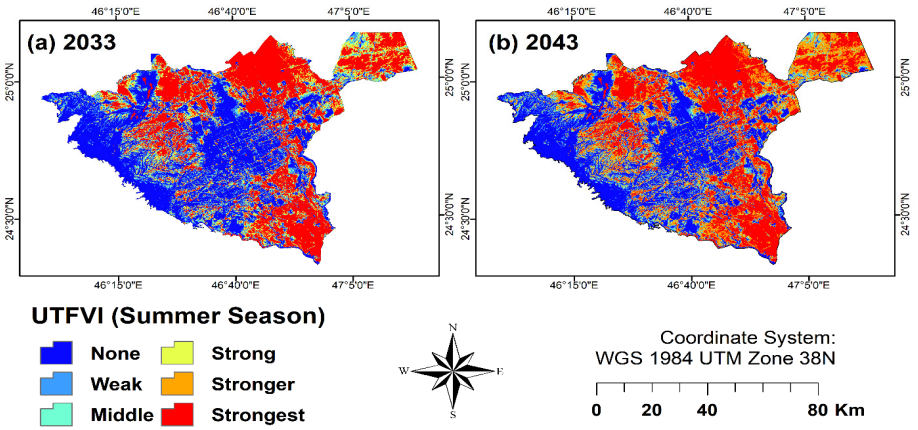
To detect possible UHI implications in the research region, further UTFVI projections are crucial, as shown by the overall shifts in periodic thermal energy fluctuation. To predict city heat circulation by season in the future, we used an ANN model. We compared the expected and observed UTFVI distributions in 2023 and used RMSE and R values to see whether our predictions were accurate. As shown in Table 19, the RMSE values were 0.729 for summer and 0.743 for winter, while the R values were 0.91 and 0.89, respectively. These values indicate a strong correlation between the predicted and actual urban geothermal variation and demonstrate the ANN model's reliability for future predictions. The predicted data clearly show that high UTFVI concentrations will accumulate in urban areas with relatively low green spaces.

In Riyadh, the predictions from (Figures 14 and 15) indicate a significant shift in the UTFVI values by the year 2033. The data show that the difference between the UTFVI values in summer and winter will be minimal, covering about 2939 km^2, or approximately 28% of the area. This suggests that the ecological condition will slightly deteriorate, affecting around 2893 km^2, which is over 30% of the city during the winter season. This indicates that the UTFVI values will be very low over roughly 30% of both seasons. Looking ahead to 2043, the prediction data indicate that summer and winter will exhibit very weak value relationships over about 32% of the season. Examining the middle or stronger range of values, the middle range will occupy only 337.34 km^2 in the summer of 2033. Additionally,

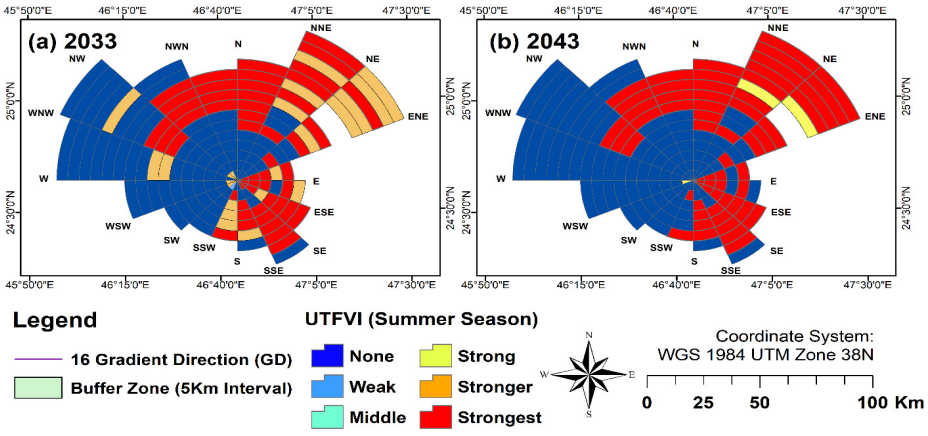
a very small area, about 81.77 km^2, will fall within the middle range value, and vice versa. Furthermore, the strongest readings of UTFVI, those at 0.02 or higher, will cover areas of 1680 km^2 and 2745 km^2 in 2033.

Table 19. For the years 2023 and 2033, the study area's seasonal UTFVI.

Year	UTFVI	None	Weak	Middle	Strong	Stronger	Strongest
	Ranges	<0	0–0.005	0.005–0.010	0.010–0.015	0.015–0.020	>0.020
2033	Summer	2939.37	334.06	337.73	336.79	341.9	1680.039
	Winter	2893.74	75.49	81.872	86.734	86.324	2745.159
2043	Summer	3000.73	314.82	312.72	314.47	331.08	1695.24
	Winter	2894.25	49.26	62.499	59.685	64.864	2838.73
2023–2033	Summer	−160.66	−12.26	2.96	17.55	19.84	132.331
	Winter	124.7	−8.37	−13.882	−16.567	−13.424	−72.599
2023–2043	Summer	−222.02	6.98	27.97	39.87	30.66	117.13
	Winter	124.19	17.86	5.491	10.482	8.036	−166.17



(**VII**)



(**VIII**)

Figure 14. (**VII**) Level of predicated summer UTFVI variation and (**VIII**) directional shifts for 2033 to 2043.

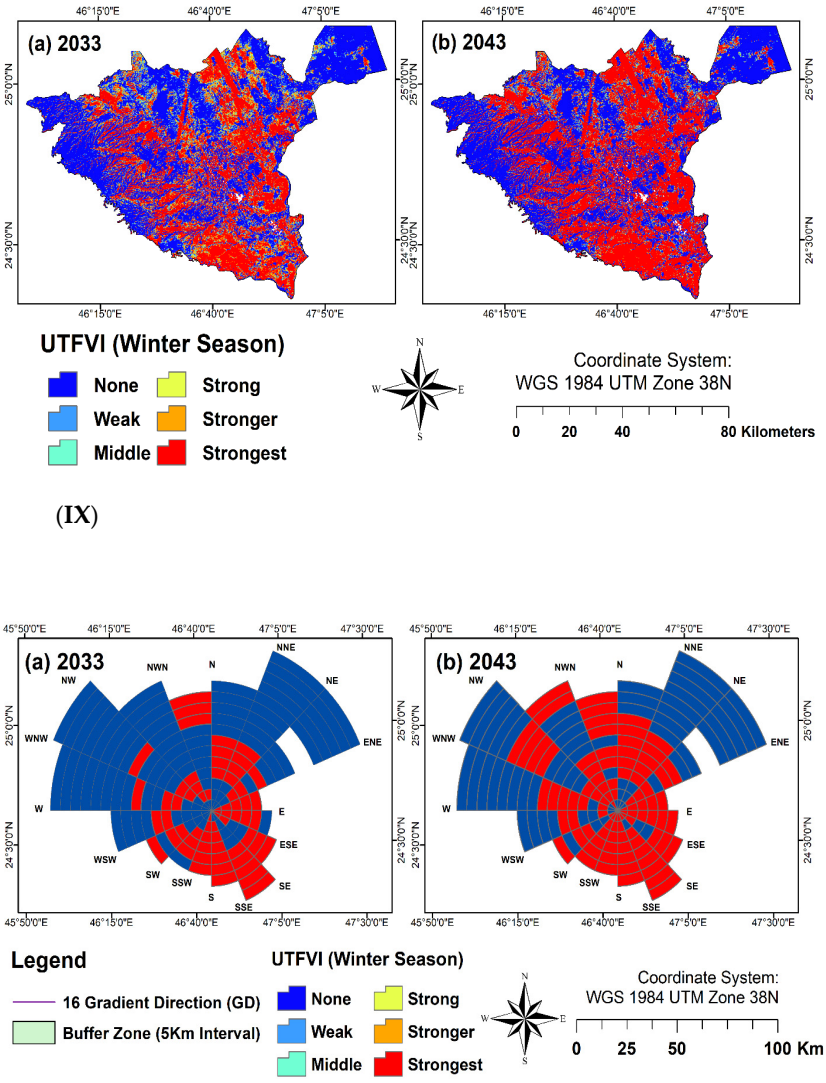


Figure 15. (**IX**) Level of Predicated winter UTFVI variation and (**X**) directional shifts for 2033 to 2043.

Similarly, for the year 2043, the areas with the strongest thermal values are expected to be 1695.24 km^2 and 2838.73 km^2. This indicates a substantial increase in the areas affected by high UTFVI values over the decade. The projected data underscores the growing urban heat island effect in Riyadh, highlighting the need for urgent mitigation strategies to address the anticipated environmental and health impacts. The significant increase in areas with low and strong geothermal variation values suggests that, without intervention, the city's ecological condition will continue to decline, further exacerbating the challenges posed by climate change and urbanization.

The heat islands that these buildings produce have a significant influence on human health, the environment of the city, and the city's capacity to maintain itself [71,72]. This is despite the fact that these structures are an essential part of urban life. Several measures can be implemented in order to significantly mitigate the effects of UTFVI and UHI in any given region [73,74]. These solutions have the potential to significantly lessen the negative effects that urban heat islands have.

4. Discussion

4.1. Urbanization and Thermal Stress

The rapid urbanization of Riyadh over the past three decades has caused significant changes in LULC, resulting in considerable thermal stress, as evidenced by the increased UHI effects. Our findings indicate that built-up areas expanded from 13.5% in 1993 to 19.5% in 2023. Similar patterns have been reported in other rapidly urbanizing arid cities. For example, studies in Jeddah reported built-up expansion from approximately 16% to 22% between 1990 and 2020, while Islamabad experienced an increase from about 11% to 18% during a comparable period, accompanied by significant reductions in vegetation cover and intensified UHI conditions [75]. Compared with these cities, Riyadh demonstrates a slightly faster thermal response to urban expansion, likely due to its extremely arid climate and limited natural vegetation cover.

The UTFVI analysis further highlights this intensification. In Riyadh, approximately 87.52% of the city experienced surface temperatures between 43 °C and 48 °C by 2023, compared to only 1.38% in 1993. In contrast, similar studies conducted in other arid cities such as Phoenix (USA) and Abu Dhabi reported that around 60–70% of urban areas fall within comparable high-thermal-stress categories [76]. This indicates that Riyadh experiences relatively higher thermal stress compared to several other arid-region cities. These findings emphasize the urgent need for targeted urban planning interventions to mitigate environmental degradation. Strategies such as increasing green infrastructure, enhancing urban vegetation, and improving urban design to promote airflow and heat dissipation should be prioritized to reduce the UHI effect and improve urban thermal comfort.

4.2. Seasonal Temperature Variations

The seasonal temperature variations over the past three decades reveal a consistent rise in both summer and winter temperatures, highlighting a year-round warming trend. Between 1993 and 2023, summer temperatures in Riyadh increased from 56.73 °C to 59.89 °C, which mirrors similar trends observed in other cities in arid regions, such as Wuhan, China, and Islamabad, Pakistan, where urban expansion has driven temperature rises due to the increased prevalence of heat-retaining materials. This increase in summer LST, largely attributed to the reduction in green spaces and the expansion of impervious surfaces like asphalt and concrete, has compounded the thermal flux in Riyadh's urban core. The lowest temperature deviations are frequently located in the dense urban core, while the most extreme thermal stress occurs on the barren outskirts. This spatial pattern indicates the presence of a daytime Surface Urban Cool Island (SUCI) or Urban Oasis effects, a well-documented phenomenon in desert cities [76]. Landsat imagery captures daytime surface temperatures; the surrounding desert sand possesses low thermal inertia and lacks moisture, causing it to heat up rapidly under intense solar radiation. In contrast, the urban core is mitigated by the shadows of tall buildings, localized irrigated vegetation, and concrete infrastructure that absorbs heat more slowly during the day [77]. Consequently, in the ANN predictive models for 2033 and 2043, as the built-up area expands outward into the desert, this daytime cooling footprint expands concurrently. While the true UHI in desert cities is most pronounced at night when the urban infrastructure slowly releases its stored heat, the daytime dynamics modeled here highlight the extreme daytime thermal hostility of the surrounding unmanaged desert environment.

Winter temperatures have also risen, with the highest average winter temperature increasing from 30.75 °C in 1993 to 32.33 °C in 2023. Although the increase in winter LST is less pronounced than in summer, this uniform warming across seasons has significant implications for the city's climate resilience. The warming trend during winter months reduces the seasonal relief typically associated with cooler periods and increases

energy consumption for cooling even during traditionally milder weather. These findings align with previous research indicating that urbanization in arid environments leads to a reduction in climate seasonality and exacerbates the thermal stress on urban populations.

4.3. Policy Implications

Given the findings of this study, vegetation has been shown to play a vital role in moderating LST by providing shade, absorbing carbon, and cooling the urban environment through evapotranspiration. The success of urban greening programs in cities like Jeddah and other parts of Saudi Arabia suggests that similar interventions could be effective in Riyadh.

Moreover, adopting reflective materials in building designs, enhancing ventilation through optimized urban layouts, and prioritizing eco-friendly infrastructure such as green roofs could significantly reduce the thermal load in densely populated areas. These strategies have been implemented successfully in cities like the Po Valley in Italy and in parts of China, where LST reductions were achieved through the introduction of sustainable urban planning measures. Riyadh could benefit from similar interventions, which would not only reduce urban heat but also improve the city's overall livability and ecological sustainability.

4.4. Implications and Future Research

The predictive models used in this study, particularly the ANN, proved reliable and forecasting UTFVI changes; however, the further refinement of these models is essential to increase their accuracy and relevance. Future research should focus on incorporating higher-resolution satellite data, such as those obtained from multi-sensor platforms, to provide a more detailed understanding of localized thermal variations within Riyadh. By integrating real-time data collection and enhancing model precision, urban planners can better anticipate the effects of land use changes on thermal dynamics, allowing for more effective interventions.

The socioeconomic impacts of rising temperatures should also be a key area of focus for future research. As observed in other developing cities such as Rajshahi, Bangladesh, lower-income neighborhoods are often disproportionately affected by UHI effects due to inadequate infrastructure and a lack of access to cooling technologies. Riyadh's policymakers must ensure that climate adaptation strategies are inclusive and equitable, addressing the needs of vulnerable populations who are most at risk from escalating thermal stress.

Furthermore, the projected urban expansion by 2043, which is expected to result in a 25.28% increase in developed areas, raises significant concerns about the city's long-term sustainability. Without immediate intervention, the continued reduction in vegetated areas and the expansion of impervious surfaces will exacerbate thermal stress and accelerate environmental degradation. Future studies should explore integrative solutions that combine advanced remote sensing, machine learning, and community-based urban planning to promote sustainable urban development while mitigating the effects of rapid urbanization.

4.5. Model Uncertainties and Limitations

While the machine learning framework utilized in this study demonstrates robust predictive capabilities based on historical trends, the projections for 2033 and 2043 are inherently extrapolative and subject to several interconnected uncertainties. First, the models are constrained by data acquisition limitations; inherent anomalies in LST retrieval such as atmospheric absorption, cloud contamination, and emissivity estimation errors introduce baseline uncertainties. Similarly, the LULC classification achieved overall accuracies of 83% to 85%. While highly acceptable for historical analysis, these minor misclassifications inevitably propagate through the CA-ANN and ANN algorithms, potentially compounding the error margins in the 10- and 20-year forecasts.

Second, the forecasting models rely on the fundamental assumption that the spatial driving forces, transition rules, and urbanization rates observed between 1993 and 2023 will remain relatively constant. Consequently, the models do not explicitly account for accelerating global macro-climatic shifts beyond historical baselines. Most importantly, the projections do not model abrupt shifts in local policy or environmental management. For instance, ambitious ongoing national strategies, such as the Saudi Vision 2030 and the Green Riyadh initiative, aim to drastically increase urban vegetation, plant millions of trees, and alter sustainable infrastructure trajectories. Because our model extrapolates past behaviors (which saw a net decrease in vegetation), it represents a "business-as-usual" baseline scenario of unchecked urban thermal expansion. Therefore, these projections should be interpreted as probabilistic warnings of what will occur without intervention, thereby reinforcing the critical necessity of the sustainable policies currently being mobilized in Riyadh.

5. Conclusions

This study demonstrates the effectiveness of machine learning models in assessing and predicting seasonal variations in the Urban Thermal Field Variation Index (UTFVI) for Riyadh, Saudi Arabia, highlighting the environmental impacts of rapid urbanization from 1993 to 2023. The city's urban areas are projected to expand to 1509.41 km^2 by 2043, intensifying thermal stress, with summer and winter temperatures expected to rise to 61.52 °C and 34.48 °C, respectively. The UTFVI analysis shows a clear increase in weak thermal field zones, indicating growing ecological vulnerability. The results underscore the potential of neural networks to forecast critical areas of concern and provide actionable insights for sustainable urban planning. Overall, the findings emphasize the importance of integrating climate-aware design and urban management strategies to enhance ecological resilience and improve living conditions in rapidly growing arid cities. Finally, this research serves as an important resource for policymakers, urban planners, and environmental scientists who are dedicated to the development of urban environments that are both resilient and sustainable.

Author Contributions: Conceptualization, M.T.M.; methodology M.T.M., R.R. and K.R.R.; software: M.T.M., R.R., A.K.A. and K.R.R.; validation, M.T.M. and K.R.R.; formal analysis, M.T.M., R.R. and K.R.R.; investigation, M.T.M., R.R. and K.R.R.; resources, M.T.M., R.R., A.K.A. and K.R.R.; writing—original draft preparation, M.T.M., R.R., A.K.A. and K.R.R.; writing—review and editing M.T.M., R.R., A.K.A. and K.R.R.; visualization, M.T.M., R.R. and K.R.R.; supervision: M.T.M. and K.R.R.; project administration M.T.M. and K.R.R.; funding acquisition, A.K.A. and K.R.R. All authors have read and agreed to the published version of the manuscript.

Funding: This research received no external funding.

Institutional Review Board Statement: Not applicable.

Informed Consent Statement: Not applicable.

Data Availability Statement: The raw data supporting the conclusions of this article will be made available by the authors on request.

Acknowledgments: The authors sincerely acknowledge USGS and NASA for providing open access to Landsat and related geospatial products.

Conflicts of Interest: The authors declare no conflicts of interest.

Appendix A

Table A1. Confusion matrices used for accuracy assessment of LULC classification for the key study years.

Year	Class	Vegetation	Barren Land	Built-Up	Total Map	User Accuracy	Producer Accuracy
1993	Vegetation	445	23	41	509	86.00%	89.00%
	Barren land	20	445	34	499	88.00%	89.00%
	Built-up	35	32	425	492	85.00%	85.00%
	Total reference	500	500	500	1500		
	Accuracy	OA: 85.2%	Kappa: 86.2%				
2003	Vegetation	440	30	45	515	88.00%	88.00%
	Barren land	30	430	55	515	86.00%	86.00%
	Built-up	30	40	400	470	88.00%	80.00%
	Total reference	500	500	500	1500		
	Accuracy	OA: 84.2%	Kappa: 88.1%				
2013	Vegetation	425	61	6	492	88.00%	85.00%
	Barren land	24	425	49	498	87.00%	85.00%
	Built-up	51	14	445	510	89.00%	89.00%
	Total reference	500	500	500	1500		
	Accuracy	OA: 85.7%	Kappa: 89.3%				
2023	Vegetation	440	30	42	512	86.00%	88.00%
	Barren land	28	445	33	506	88.00%	89.00%
	Built-up	32	25	425	482	88.00%	85.00%
	Total reference	500	500	500	1500		
	Accuracy	OA: 83.4%	Kappa: 87.1%				

Table A2. Summary of LULC proportions, mean LST, and UTFVI class distribution for the selected study years.

Year	Season	LULC Proportions (%)			Mean LST (°C)	UTFVI Class Proportions (%)					
		Vegetation	Barren	Built-Up		None	Weak	Middle	Strong	Stronger	Strongest
1993	Summer	0.77	88.31	10.83	40.05	44.73	6.55	6.94	6.93	6.4	28.44
	Winter	0.77	88.31	10.83	22.35	50.43	2.41	2.29	2.3	2.51	40.06
2003	Summer	0.67	85.75	13.51	41.22	45.28	6.7	7.33	7.1	6.36	27.22
	Winter	0.67	85.75	13.51	22.63	46.56	3.23	2.55	4.01	2.69	40.95
2013	Summer	1.12	83.73	15.07	43.94	50.11	6.96	6.84	6.34	5.73	24.01
	Winter	1.12	83.73	15.07	23.35	46.25	2.69	2.75	2.86	2.96	42.49
2023	Summer	0.67	79.61	19.56	44.08	46.55	5.39	5.71	5.94	6.06	30.36
	Winter	0.67	79.61	19.56	24.48	50.56	1.12	1.14	1.18	1.22	44.77

Appendix B

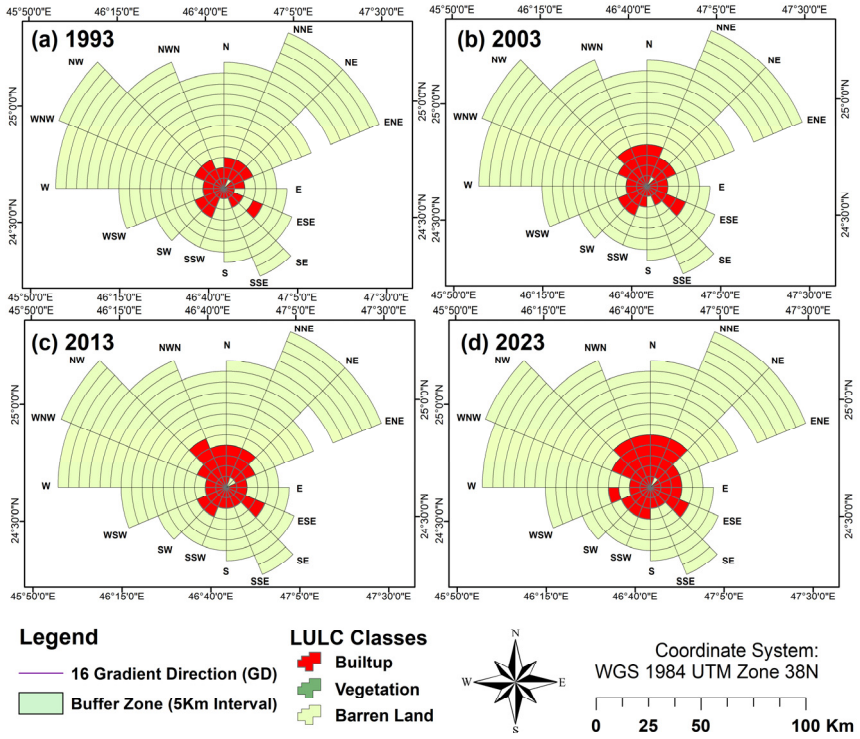


Figure A1. Directional map of (**a**) 1993, (**b**) 2003, (**c**) 2013, and (**d**) 2023.

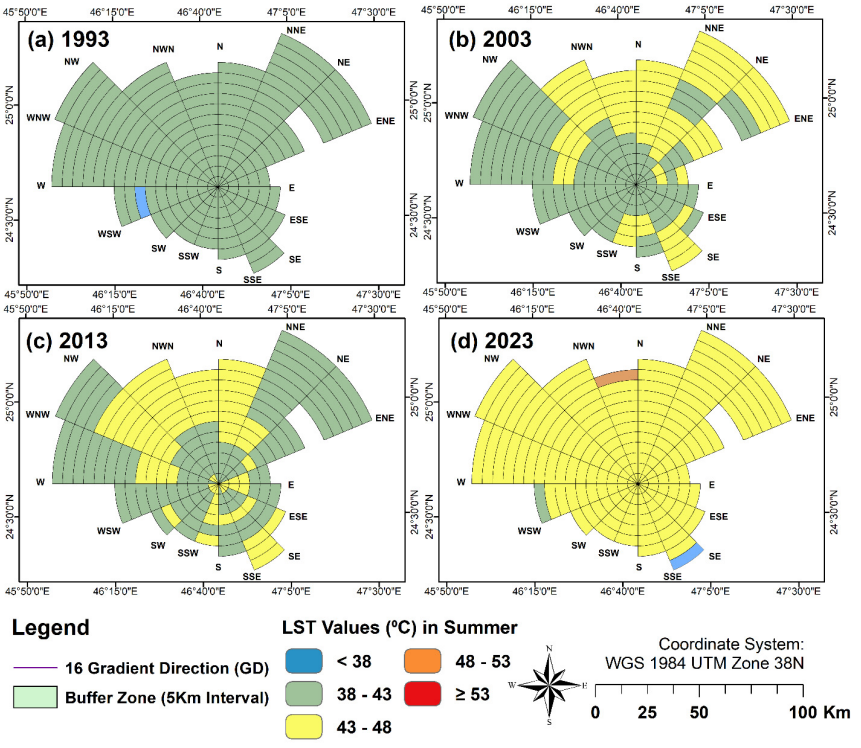


Figure A2. Summer LST change in (**a**) 1993, (**b**) 2003, (**c**) 2013, and (**d**) 2023.

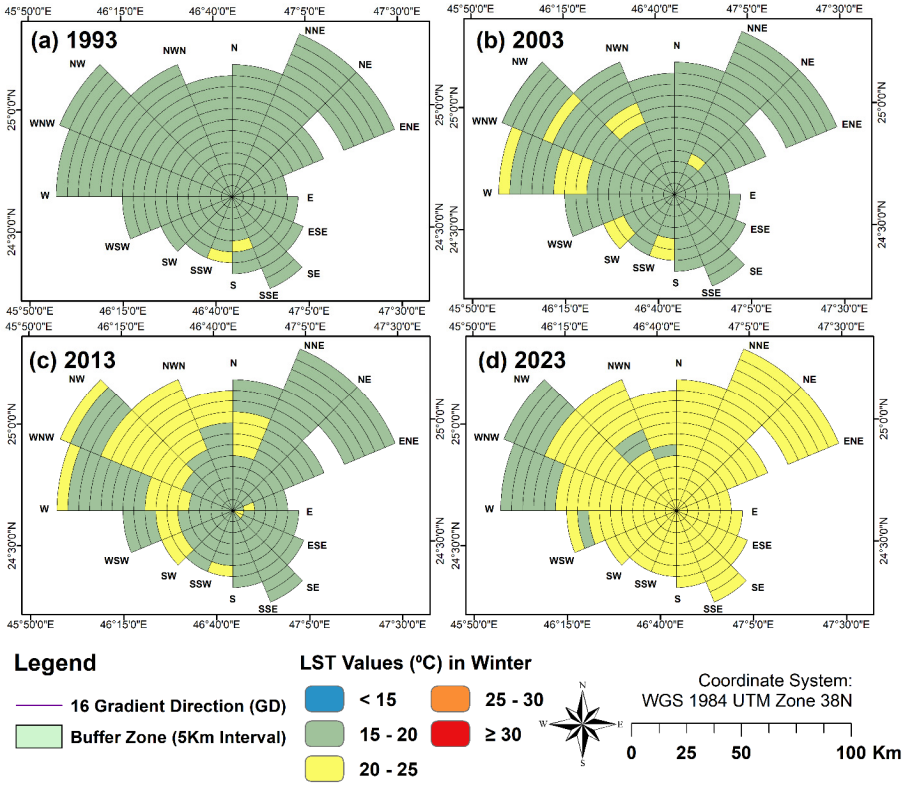


Figure A3. Winter directional variation in years of (**a**) 1993, (**b**) 2003, (**c**) 2013, and (**d**) 2023.

References

1. Chapman, S.; Watson, J.E.M.; Salazar, A.; Thatcher, M.; McAlpine, C.A. The impact of urbanization and climate change on urban temperatures: A systematic review. *Landsc. Ecol.* **2017**, *32*, 1921–1935. [CrossRef]
2. Miky, Y.H. Remote sensing analysis for surface urban heat island detection over Jeddah, Saudi Arabia. *Appl. Geomat.* **2019**, *11*, 243–258. [CrossRef]
3. Miky, Y.; Al Shouny, A.; Abdallah, A. Studying the Impact of Urban Management Strategies and Spatiotemporal Dynamics of LULC on Land Surface Temperature and SUHI Formation in Jeddah, Saudi Arabia. *Sustainability* **2023**, *15*, 15316. [CrossRef]
4. Hegazy, I.R.; Qurnfulah, E.M. Thermal comfort of urban spaces using simulation tools exploring street orientation influence of on the outdoor thermal comfort: A case study of Jeddah, Saudi Arabia. *Int. J. Low-Carbon Technol.* **2020**, *15*, 594–606. [CrossRef]
5. Rahman, M.S.; Mohiuddin, H.; Kafy, A.-A.; Sheel, P.K.; Di, L. Classification of cities in Bangladesh based on remote sensing derived spatial characteristics. *J. Urban Manag.* **2019**, *8*, 206–224. [CrossRef]
6. Tang, J.; Di, L.; Rahman, M.S.; Yu, Z. Spatial–temporal landscape pattern change under rapid urbanization. *J. Appl. Remote Sens.* **2019**, *13*, 024503. [CrossRef]
7. Huang, Q.; Huang, J.; Yang, X.; Fang, C.; Liang, Y. Quantifying the seasonal contribution of coupling urban land use types on Urban Heat Island using Land Contribution Index: A case study in Wuhan, China. *Sustain. Cities Soc.* **2019**, *44*, 666–675. [CrossRef]
8. Al Kafy, A.; Rahman, M.S.; Faisal, A.-A.; Hasan, M.M.; Islam, M. Modelling future land use land cover changes and their impacts on land surface temperatures in Rajshahi, Bangladesh. *Remote Sens. Appl.* **2020**, *18*, 100314. [CrossRef]
9. Hassan, T.; Zhang, J.; Prodhan, F.A.; Sharma, T.P.P.; Bashir, B. Surface Urban Heat Islands Dynamics in Response to LULC and Vegetation across South Asia (2000–2019). *Remote Sens.* **2021**, *13*, 3177. [CrossRef]
10. Tomlinson, C.J.; Chapman, L.; Thornes, J.E.; Baker, C.J. Including the urban heat island in spatial heat health risk assessment strategies: A case study for Birmingham, UK. *Int. J. Health Geogr.* **2011**, *10*, 42. [CrossRef]
11. Wang, H.; Zhang, Y.; Tsou, J.; Li, Y. Surface Urban Heat Island Analysis of Shanghai (China) Based on the Change of Land Use and Land Cover. *Sustainability* **2017**, *9*, 1538. [CrossRef]
12. Sejati, A.W.; Buchori, I.; Rudiarto, I. The spatio-temporal trends of urban growth and surface urban heat islands over two decades in the Semarang Metropolitan Region. *Sustain. Cities Soc.* **2019**, *46*, 101432. [CrossRef]
13. Singh, J.; Sekharan, S.; Karmakar, S.; Ghosh, S.; Zope, P.E.; Eldho, T.I. Spatio-temporal analysis of sub-hourly rainfall over Mumbai, India: Is statistical forecasting futile? *J. Earth Syst. Sci.* **2017**, *126*, 38. [CrossRef]

14. Tran, D.X.; Pla, F.; Latorre-Carmona, P.; Myint, S.W.; Caetano, M.; Kieu, H.V. Characterizing the relationship between land use land cover change and land surface temperature. *ISPRS J. Photogramm. Remote Sens.* **2017**, *124*, 119–132. [CrossRef]
15. Losiri, C.; Nagai, M.; Ninsawat, S.; Shrestha, R. Modeling Urban Expansion in Bangkok Metropolitan Region Using Demographic–Economic Data through Cellular Automata-Markov Chain and Multi-Layer Perceptron-Markov Chain Models. *Sustainability* **2016**, *8*, 686. [CrossRef]
16. Al-Ageili, M.; Mouhoub, M.; Piwowar, J. Remote Sensing, Gis and Cellular Automata for Urban Growth Simulation. *Comput. Inf. Sci.* **2017**, *10*, 38. [CrossRef]
17. Shatnawi, N.; Qdais, H.A. Mapping urban land surface temperature using remote sensing techniques and artificial neural network modelling. *Int. J. Remote Sens.* **2019**, *40*, 3968–3983. [CrossRef]
18. Oliver, T.H.; Roy, D.B. The pitfalls of ecological forecasting. *Biol. J. Linn. Soc.* **2015**, *115*, 767–778. [CrossRef]
19. Gómez, J.A.; Guan, C.; Tripathy, P.; Duque, J.C.; Passos, S.; Keith, M.; Liu, J. Analyzing the Spatiotemporal Uncertainty in Urbanization Predictions. *Remote Sens.* **2021**, *13*, 512. [CrossRef]
20. AlQahtany, A. People's perceptions of sustainable housing in developing countries: The case of Riyadh, Saudi Arabia. *Hous. Care Support* **2020**, *23*, 93–109. [CrossRef]
21. Mansour, S. Spatial analysis of public health facilities in Riyadh Governorate, Saudi Arabia: A GIS-based study to assess geographic variations of service provision and accessibility. *Geo-Spat. Inf. Sci.* **2016**, *19*, 26–38. [CrossRef]
22. Alvares, C.A.; Stape, J.L.; Sentelhas, P.C.; de Moraes Gonçalves, J.L.; Sparovek, G. Köppen's climate classification map for Brazil. *Meteorol. Z.* **2013**, *22*, 711–728. [CrossRef] [PubMed]
23. Zhao, L.; Oppenheimer, M.; Zhu, Q.; Baldwin, J.W.; Ebi, K.L.; Bou-Zeid, E.; Guan, K.; Liu, X. Interactions between urban heat islands and heat waves. *Environ. Res. Lett.* **2018**, *13*, 034003. [CrossRef]
24. Vanderbilt, D. The Mukaab: Inside Saudi Arabia's $50 Billion Cube and Why It Was Suspended. 2026. Available online: https://vision2030.ai/ (accessed on 8 March 2026).
25. Mazzetto, S.; Furlan, R.; Awwaad, R. Sustainable Urban Renewal: Planning Transit-Oriented Development (TOD) in Riyadh. *Sustainability* **2025**, *17*, 4310. [CrossRef]
26. Khogali, H.A.M. Development of Heritage Places under Unesco Guidelines Case Study: Al Maliha Neighbourhood in Riyadh City. *Int. J. Glob. Sustain.* **2017**, *1*, 18. [CrossRef]
27. Mohajerani, A.; Bakaric, J.; Jeffrey-Bailey, T. The urban heat island effect, its causes, and mitigation, with reference to the thermal properties of asphalt concrete. *J. Environ. Manag.* **2017**, *197*, 522–538. [CrossRef]
28. Gutman, G.; Huang, C.; Chander, G.; Noojipady, P.; Masek, J.G. Assessment of the NASA–USGS Global Land Survey (GLS) datasets. *Remote Sens. Environ.* **2013**, *134*, 249–265. [CrossRef]
29. Roy, D.P.; Ju, J.; Kline, K.; Scaramuzza, P.L.; Kovalskyy, V.; Hansen, M.; Loveland, T.R.; Vermote, E.; Zhang, C. Web-enabled Landsat Data (WELD): Landsat ETM+ composited mosaics of the conterminous United States. *Remote Sens. Environ.* **2010**, *114*, 35–49. [CrossRef]
30. Fariha, J.N.; Miah, M.T.; Limon, Z.A.; Alsulamy, S.; Al Kafy, A.; Rahman, S.N. Quantifying spatial dynamics of urban sprawl for climate resilience sustainable natural resource management by utilizing geostatistical and remote sensing techniques. *Theor. Appl. Climatol.* **2024**, *155*, 6307–6349. [CrossRef]
31. Miah, M.T.; Fariha, J.N.; Al Kafy, A.; Islam, R.; Biswas, N.; Duti, B.M.; Fattah, A.; Alsulamy, S.; Khedher, K.M.; Salem, M.A. Exploring the nexus between land cover change dynamics and spatial heterogeneity of demographic trajectories in rapidly growing ecosystems of south Asian cities. *Ecol. Indic.* **2024**, *158*, 111299. [CrossRef]
32. Chakraborty, A.; Sachdeva, K.; Joshi, P.K. A Reflection on Image Classifications for Forest Ecology Management: Towards Landscape Mapping and Monitoring. In *Handbook of Neural Computation*; Elsevier: Amsterdam, The Netherlands, 2017; pp. 67–85. [CrossRef]
33. Arifeen, H.M.; Phoungthong, K.; Mostafaeipour, A.; Yuangyai, N.; Yuangyai, C.; Techato, K.; Jutidamrongphan, W. Determine the Land-Use Land-Cover Changes, Urban Expansion and Their Driving Factors for Sustainable Development in Gazipur Bangladesh. *Atmosphere* **2021**, *12*, 1353. [CrossRef]
34. Foody, G.M. Explaining the unsuitability of the kappa coefficient in the assessment and comparison of the accuracy of thematic maps obtained by image classification. *Remote Sens. Environ.* **2020**, *239*, 111630. [CrossRef]
35. Tassi, A.; Vizzari, M. Object-Oriented LULC Classification in Google Earth Engine Combining SNIC, GLCM, and Machine Learning Algorithms. *Remote Sens.* **2020**, *12*, 3776. [CrossRef]
36. Qian, Y.; Zeng, G.; Pan, Y.; Liu, Y.; Zhang, L.; Li, K. A Prediction Model for High Risk of Positive RT-PCR Test Results in COVID-19 Patients Discharged from Wuhan Leishenshan Hospital, China. *Front. Public Health* **2021**, *9*, 778539. [CrossRef]
37. Liu, Y.; Qian, J.; Yue, H. Comparison and evaluation of different dryness indices based on vegetation indices-land surface temperature/albedo feature space. *Adv. Space Res.* **2021**, *68*, 2791–2803. [CrossRef]
38. Heagerty, P.J.; Lumley, T.; Pepe, M.S. Time-Dependent ROC Curves for Censored Survival Data and a Diagnostic Marker. *Biometrics* **2000**, *56*, 337–344. [CrossRef]

39. Walter, S.D. The partial area under the summary ROC curve. *Stat. Med.* **2005**, *24*, 2025–2040. [CrossRef]
40. Rasul, A.; Balzter, H.; Smith, C. Spatial variation of the daytime Surface Urban Cool Island during the dry season in Erbil, Iraqi Kurdistan, from Landsat 8. *Urban Clim.* **2015**, *14*, 176–186. [CrossRef]
41. Rozenstein, O.; Qin, Z.; Derimian, Y.; Karnieli, A. Derivation of Land Surface Temperature for Landsat-8 TIRS Using a Split Window Algorithm. *Sensors* **2014**, *14*, 5768–5780. [CrossRef]
42. Scarano, M.; Sobrino, J.A. On the relationship between the sky view factor and the land surface temperature derived by Landsat-8 images in Bari, Italy. *Int. J. Remote Sens.* **2015**, *36*, 4820–4835. [CrossRef]
43. Roy, S.; Sowgat, T.; Ahmed, M.U.; Islam, S.T.; Anjum, N.; Mondal, J.; Rahman, M.M. *Bangladesh: National Urban Policies and City Profiles for Dhaka and Khulna*; GCRF Centre for Sustainable, Healthy and Learning Cities and Neighborhood (SHLC): Glasgow, UK, 2018. Available online: https://centreforsustainablecities.ac.uk/wp-content/uploads/2018/06/Executive-Summary-Bangladesh-National-Urban-Policies-and-City-Profiles-for-Dhaka-and-Khulna.pdf (accessed on 10 January 2026).
44. Weng, Q.; Lu, D.; Schubring, J. Estimation of land surface temperature–vegetation abundance relationship for urban heat island studies. *Remote Sens. Environ.* **2004**, *89*, 467–483. [CrossRef]
45. Roy, S.; Pandit, S.; Eva, E.A.; Bagmar, S.H.; Papia, M.; Banik, L.; Dube, T.; Rahman, F.; Razi, M.A. Examining the nexus between land surface temperature and urban growth in Chattogram Metropolitan Area of Bangladesh using long term Landsat series data. *Urban Clim.* **2020**, *32*, 100593. [CrossRef]
46. Yu, X.; Guo, X.; Wu, Z. Land Surface Temperature Retrieval from Landsat 8 TIRS—Comparison between Radiative Transfer Equation-Based Method, Split Window Algorithm and Single Channel Method. *Remote Sens.* **2014**, *6*, 9829–9852. [CrossRef]
47. Avdan, U.; Jovanovska, G. Algorithm for Automated Mapping of Land Surface Temperature Using LANDSAT 8 Satellite Data. *J. Sens.* **2016**, *2016*, 1480307. [CrossRef]
48. Abutaleb, K.; Ngie, A.; Darwish, A.; Ahmed, M.; Arafat, S.; Ahmed, F. Assessment of Urban Heat Island Using Remotely Sensed Imagery over Greater Cairo, Egypt. *Adv. Remote Sens.* **2015**, *4*, 35–47. [CrossRef]
49. Liu, L.; Zhang, Y. Urban Heat Island Analysis Using the Landsat TM Data and ASTER Data: A Case Study in Hong Kong. *Remote Sens.* **2011**, *3*, 1535–1552. [CrossRef]
50. Ullah, S.; Ahmad, K.; Sajjad, R.U.; Abbasi, A.M.; Nazeer, A.; Tahir, A.A. Analysis and simulation of land cover changes and their impacts on land surface temperature in a lower Himalayan region. *J. Environ. Manag.* **2019**, *245*, 348–357. [CrossRef]
51. Santé, I.; García, A.M.; Miranda, D.; Crecente, R. Cellular automata models for the simulation of real-world urban processes: A review and analysis. *Landsc. Urban Plan.* **2010**, *96*, 108–122. [CrossRef]
52. Ullah, A.K.M.A. Bright City Lights and Slums of Dhaka city: Determinants of rural-urban migration in Bangladesh. *Migr. Lett.* **2004**, *1*, 26–41. [CrossRef]
53. Qiu, C.; Schmitt, M.; Mou, L.; Ghamisi, P.; Zhu, X. Feature Importance Analysis for Local Climate Zone Classification Using a Residual Convolutional Neural Network with Multi-Source Datasets. *Remote Sens.* **2018**, *10*, 1572. [CrossRef]
54. Mansour, S.; Al-Belushi, M.; Al-Awadhi, T. Monitoring land use and land cover changes in the mountainous cities of Oman using GIS and CA-Markov modelling techniques. *Land Use Policy* **2020**, *91*, 104414. [CrossRef]
55. Sekertekin, A.; Arslan, N.; Bilgili, M. Modeling Diurnal Land Surface Temperature on a Local Scale of an Arid Environment Using Artificial Neural Network (ANN) and Time Series of Landsat-8 Derived Spectral Indexes. *J. Atmos. Sol. Terr. Phys.* **2020**, *206*, 105328. [CrossRef]
56. Lee, S.; Jung, S.; Lee, J. Prediction Model Based on an Artificial Neural Network for User-Based Building Energy Consumption in South Korea. *Energies* **2019**, *12*, 608. [CrossRef]
57. Gilbert, K.M.; Shi, Y. Land Use/Land Cover Changes Detection in Lagos City of Nigeria Using Remote Sensing and GIS. *Adv. Remote Sens.* **2023**, *12*, 145–165. [CrossRef]
58. ID, M. Simulation and Prediction of Land Surface Temperature (LST) Dynamics within Ikom City in Nigeria Using Artificial Neural Network (ANN). *J. Remote Sens. GIS* **2015**, *5*. [CrossRef]
59. De Carvalho, R.M.; Szlafsztein, C.F. Urban vegetation loss and ecosystem services: The influence on climate regulation and noise and air pollution. *Environ. Pollut.* **2019**, *245*, 844–852. [CrossRef]
60. Klingmann, A. Rescripting Riyadh: How the capital of Saudi Arabia employs urban megaprojects as catalysts to enhance the quality of life within the city's neighborhoods. *J. Place Manag. Dev.* **2023**, *16*, 45–72. [CrossRef]
61. Rahman, M.T. Land Use and Land Cover Changes and Urban Sprawl in Riyadh, Saudi Arabia: An Analysis Using Multi-Temporal Landsat Data and Shannon's Entropy Index. *Int. Arch. Photogramm. Remote Sens. Spat. Inf. Sci.* **2016**, *XLI-B8*, 1017–1021. [CrossRef]
62. Almazroui, M.; Islam, M.N.; Jones, P.D. Urbanization effects on the air temperature rise in Saudi Arabia. *Clim. Change* **2013**, *120*, 109–122. [CrossRef]
63. Mohamed, A.; Lorestani, N.; Shabani, F. Impact of urbanization on land surface temperature: A global perspective. *Curr. Res. Environ. Sustain.* **2025**, *10*, 100315. [CrossRef]
64. Siddiqui, A.; Maske, A.B.; Khan, A.; Kar, A.; Bhatt, M.; Bharadwaj, V.; Kant, Y.; Hamdi, R. An Urban Climate Paradox of Anthropogenic Heat Flux and Urban Cool Island in a Semi-Arid Urban Environment. *Atmosphere* **2025**, *16*, 151. [CrossRef]

65. Munir, S.; Habeebullah, T.M.A.; Zamreeq, A.O.; Alfehaid, M.M.A.; Ismail, M.; Khalil, A.A.; Baligh, A.A.; Islam, M.N.; Jamaladdin, S.; Ghulam, A.S. Cooling of Maximum Temperatures in Six Saudi Arabian Cities (1994–2024)—Reversal of Urban Heat Islands. *Urban Sci.* **2025**, *9*, 445. [CrossRef]
66. Rahman, M.T. Examining and Modelling the Determinants of the Rising Land Surface Temperatures in Arabian Desert Cities: An Example from Riyadh, Saudi Arabia. *J. Settl. Spat. Plan.* **2018**, *9*, 1–10. [CrossRef]
67. Neteler, M. Estimating Daily Land Surface Temperatures in Mountainous Environments by Reconstructed MODIS LST Data. *Remote Sens.* **2010**, *2*, 333–351. [CrossRef]
68. Al Kafy, A.; Al-Faisal, A.; Hasan, M.M.; Sikdar, S.; Khan, M.H.H.; Rahman, M.; Islam, R. Impact of LULC Changes on LST in Rajshahi District of Bangladesh: A Remote Sensing Approach. *J. Geogr. Stud.* **2020**, *3*, 11–23. [CrossRef]
69. Chen, X.-L.; Zhao, H.-M.; Li, P.-X.; Yin, Z.-Y. Remote sensing image-based analysis of the relationship between urban heat island and land use/cover changes. *Remote Sens. Environ.* **2006**, *104*, 133–146. [CrossRef]
70. Dar, I.; Qadir, J.; Shukla, A. Estimation of LST from multi-sensor thermal remote sensing data and evaluating the influence of sensor characteristics. *Ann. GIS* **2019**, *25*, 263–281. [CrossRef]
71. IPCC. Mitigation of climate change. In *Contribution of Working Group III to the Fifth Assessment Report of the Intergovernmental Panel on Climate Change*; IPCC: Geneva, Switzerland, 2014.
72. Ramachandran, R.M.; Roy, P.S.; Chakravarthi, V.; Joshi, P.K.; Sanjay, J. Land use and climate change impacts on distribution of plant species of conservation value in Eastern Ghats, India: A simulation study. *Environ. Monit. Assess.* **2020**, *192*, 86. [CrossRef]
73. Yang, X.; Peng, L.L.H.; Jiang, Z.; Chen, Y.; Yao, L.; He, Y.; Xu, T. Impact of urban heat island on energy demand in buildings: Local climate zones in Nanjing. *Appl. Energy* **2020**, *260*, 114279. [CrossRef]
74. Santamouris, M. Recent progress on urban overheating and heat island research. Integrated assessment of the energy, environmental, vulnerability and health impact. Synergies with the global climate change. *Energy Build.* **2020**, *207*, 109482. [CrossRef]
75. Khan, M.S.; Ullah, S.; Sun, T.; Rehman, A.; Chen, L. Land-Use/Land-Cover Changes and Its Contribution to Urban Heat Island: A Case Study of Islamabad, Pakistan. *Sustainability* **2020**, *12*, 3861. [CrossRef]
76. Jenerette, G.D.; Harlan, S.L.; Buyantuev, A.; Stefanov, W.L.; Declet-Barreto, J.; Ruddell, B.L.; Myint, S.W.; Kaplan, S.; Li, X. Micro-scale urban surface temperatures are related to land-cover features and residential heat related health impacts in Phoenix, AZ USA. *Landsc. Ecol.* **2016**, *31*, 745–760. [CrossRef]
77. Haashemi, S.; Weng, Q.; Darvishi, A.; Alavipanah, S. Seasonal Variations of the Surface Urban Heat Island in a Semi-Arid City. *Remote Sens.* **2016**, *8*, 352. [CrossRef]

Disclaimer/Publisher's Note: The statements, opinions and data contained in all publications are solely those of the individual author(s) and contributor(s) and not of MDPI and/or the editor(s). MDPI and/or the editor(s) disclaim responsibility for any injury to people or property resulting from any ideas, methods, instructions or products referred to in the content.